

Symmetric and Baroclinic Instability in Dense Shelf Overflows

ELIZABETH YANKOVSKY AND SONYA LEGG

Program in Atmospheric and Oceanic Sciences, Princeton University, Princeton, New Jersey

(Manuscript received 3 April 2018, in final form 22 October 2018)

ABSTRACT

In this study, we revisit the problem of rotating dense overflow dynamics by performing nonhydrostatic numerical simulations, resolving submesoscale variability. Thermohaline stratification and buoyancy forcing are based on data from the Eurasian basin of the Arctic Ocean, where overflows are particularly crucial to the exchange of dense water between shelves and deep basins, yet have been studied relatively little. A nonlinear equation of state is used, allowing proper representation of thermohaline structure and mixing. We examine three increasingly complex scenarios: nonrotating 2D, rotating 2D, and rotating 3D. The nonrotating 2D case behaves according to known theory: the gravity current descends alongslope until reaching a relatively shallow neutral buoyancy level. However, in the rotating cases, we have identified novel dynamics: in both 2D and 3D, the submesoscale range is dominated by symmetric instability (SI). Rotation leads to geostrophic adjustment, causing dense water to be confined within the forcing region longer and attain a greater density anomaly. In the 2D case, Ekman drainage leads to descent of the geostrophic jet, forming a highly dense alongslope front. Beams of negative Ertel potential vorticity develop parallel to the slope, initiating SI and vigorous mixing in the overflow. In 3D, baroclinic eddies are responsible for cross-isobath dense water transport, but SI again develops along the slope and at eddy edges. Remarkably, through two different dynamics, the 2D SI-dominated case and 3D eddy-dominated case attain roughly the same final water mass distribution, highlighting the potential role of SI in driving mixing within certain regimes of dense overflows.


1. Introduction

The term “overflow” refers to the buoyancy-driven descent of dense water formed through cooling, freezing, or evaporation in shallow regions of the World Ocean, such as continental shelves and marginal seas. As dense water descends into the ocean interior, typically as a terrain-following gravity current along slopes or sills (Shapiro et al. 2003), it undergoes mixing, entrains ambient water, and serves as a conduit for irreversible exchange and ventilation of the otherwise relatively quiescent abyssal ocean. Dense overflows feed intermediate and deep water masses, including North Atlantic Deep Water and Antarctic Bottom Water, and thus are substantial contributors to oceanic circulation and climate (Killworth 1983). Examples occur worldwide—for instance, in the Antarctic shelves (Bergamasco et al. 2002), Mediterranean outflow (Price

et al. 1993), Red Sea (Murray and Johns 1997), and Nordic Seas (Eldevik et al. 2009).

In this work, we focus on perhaps the most striking case: the Arctic Ocean, where continental shelves comprise approximately 53% of the total surface area (Jakobsson 2002) and are subject to intense atmospheric cooling and sea ice formation with associated brine rejection during fall and winter. Highly cold and saline shelf water is formed, and the resulting overflows are inferred to ventilate the deepest portions of the Arctic (Aagaard et al. 1985). Additionally, shelf overflows strengthen the Arctic halocline—a layer between 50- and 200-m depth that buffers sea ice from the underlying warm Atlantic inflow layer, the heat reservoir of which is capable of melting the entire Arctic ice pack (Aagaard et al. 1981). As observations of Arctic shelf overflows are indirect and sparse, numerical modeling remains a reasonable alternative to studying their dynamics. Because of the rapidly changing nature of the modern Arctic, understanding exchange processes and representing them properly in climate models is crucial.

Present theory, predominantly based on idealized hydrostatic simulations with ~ 1 -km horizontal resolutions,

 Denotes content that is immediately available upon publication as open access.

Corresponding author: Elizabeth Yankovsky, eay@princeton.edu

DOI: 10.1175/JPO-D-18-0072.1

© 2018 American Meteorological Society. For information regarding reuse of this content and general copyright information, consult the [AMS Copyright Policy](https://www.ametsoc.org/PUBSReuseLicenses) (www.ametsoc.org/PUBSReuseLicenses).

suggests that bottom friction and mesoscale baroclinic eddies are the dominant mechanisms in transporting dense Arctic shelf water downslope and driving mixing (Gawarkiewicz and Chapman 1995; Gawarkiewicz 2000; Wobus et al. 2011). However, the role of submesoscale instabilities, particularly symmetric instability (SI), has not been examined in the context of overflows. SI is ubiquitous in both the atmosphere and ocean at frontal zones and has been shown to be highly efficient in removing kinetic energy from geostrophic currents (Taylor and Ferrari 2010). A flow becomes unstable when Ertel potential vorticity q is opposite in sign to the Coriolis parameter f (Holton 2004):

$$q = (f\hat{\mathbf{k}} + \nabla \wedge \mathbf{u}) \cdot \nabla b. \quad (1)$$

Here, \mathbf{u} is the three-dimensional (3D) velocity vector, buoyancy is defined as $b = -g\rho/\rho_0$, g is acceleration due to gravity, and ρ is potential density referenced to 0 dbar. Depending on the signs and magnitudes of the components in Eq. (1) that lead to the instability criterion $fq < 0$ being satisfied, various forms of instability are possible: gravitational, inertial, symmetric, or hybrids among these (Thomas et al. 2013). SI is characterized by large magnitudes of vertical shear and horizontal density gradients (Hoskins 1974). Given the strong geostrophic shear and density fronts arising in bottom-trapped overflows, we hypothesize SI has a significant role in overflow dynamics. Allen and Newberger (1998) have theoretically demonstrated the susceptibility of topographic flows and bottom boundary layers to SI. Further, there is growing observational evidence emphasizing the role of submesoscale instabilities and topographically generated turbulence in global circulation. Ruan et al. (2017) identify SI-driven mixing within the Antarctic Circumpolar Current important to the closure of Southern Ocean overturning. Topographically generated submesoscale instabilities have also been proposed as a new route for energy dissipation of geostrophic flows such as the Gulf Stream (Gula et al. 2016) and the California Undercurrent (Molemaker et al. 2015).

Here, we apply the nonhydrostatic Massachusetts Institute of Technology general circulation model (MITgcm; Marshall et al. 1997) to perform simulations of Arctic shelf overflows, resolving a wide spectrum of submesoscale variability. To distinguish between different instability regimes, we consider three progressively complex scenarios: 2D without rotation, 2D with rotation, and 3D with rotation. Initial temperature and salinity stratification, as well as the thermal and haline forcing values, are based on conditions in the Eurasian basin of the Arctic. A nonlinear equation of state is used, yielding realistic mixing and thermohaline structure.

The primary goal of this work is to identify the physical processes responsible for transporting dense water offshore and downslope and to examine how tracer properties of the overflow and surrounding water are modified through mixing. Our paper is organized as follows: section 2 details model setup, section 3 describes the nonrotating 2D case driven by gravitational instability, section 4 describes the rotating 2D case dominated by SI, and section 5 describes the rotating 3D case dominated by baroclinic eddies. In section 6, we compare the water mass transformation, entrainment, and energetic pathways between the rotating 2D and 3D cases. We find that 1) through different mixing pathways, the two cases attain roughly the same water mass distribution for a given forcing, and 2) SI dominates the submesoscale range of both cases.

2. Model description

The z -coordinate MITgcm (Marshall et al. 1997) is used to solve the nonhydrostatic, Boussinesq Navier–Stokes equations in three otherwise identical configurations: 2D with and without rotation and 3D with rotation. For rotating simulations, we use an f -plane approximation, with $f = 1.43 \times 10^{-4} \text{ s}^{-1}$. In solving the density equation, a nonlinear equation of state (McDougall et al. 2003) is used. To parameterize subgrid-scale processes, we use a Laplacian viscosity and choose constant vertical and horizontal viscosity coefficients so that the grid Reynolds number is near order one, preventing buildup of energy at the grid scale. The horizontal viscosity is $\nu_H = 2.5 \text{ m}^2 \text{ s}^{-1}$, and vertical viscosity is $\nu_Z = 0.01 \text{ m}^2 \text{ s}^{-1}$. Explicit salt and temperature diffusivities are set to zero, and a third-order direct space–time advection scheme with a flux limiter is utilized, leading to numerical diffusion. We tested explicit diffusivities of 1/1000 of the viscosity values and found negligible differences with the numerical diffusion case. Simulations are performed to 60 days, and the lower forcing cases are extended to 120 days. The across-shore (x direction) domain length is 75 km, and depth ranges from 40 to 2500 m (Fig. 1). The 3D simulations have uniform topography alongshore (y direction), with a width of 100 km—significantly larger than the Rossby deformation radius [$L_R = NH/(\pi f) \approx 5 \text{ km}$; where N is buoyancy frequency and H is depth] so that baroclinic instabilities are uninhibited. Variable grid resolution is employed to focus on the shelf/shelfbreak region. Resolution varies from 10 to 40 m in z and from 110 to 130 m in x , and it is 110 m in y (in 3D). There is a no-slip boundary condition at the bottom and coastal wall of the domain, a free surface, a 2-km sponge boundary at the

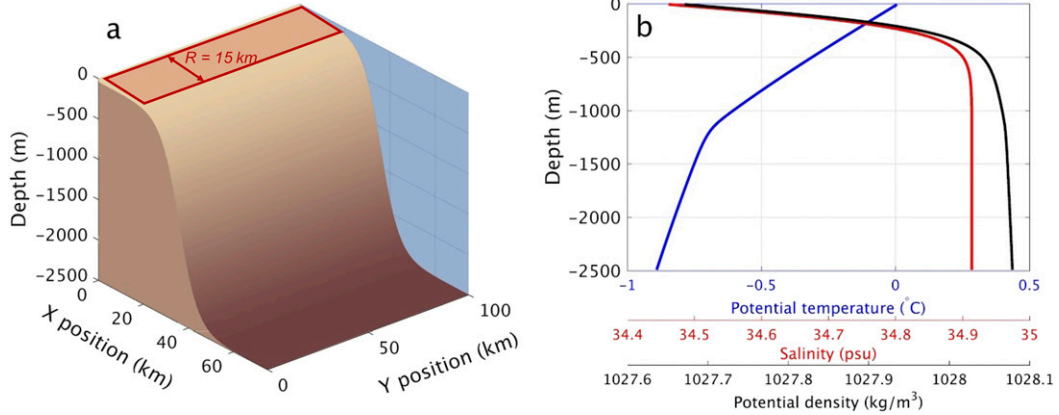


FIG. 1. (a) Model domain, with forcing region (offshore length $R = 15$ km) shaded in red; (b) initial profiles of salinity, potential temperature, and potential density, referenced to the surface (0 dbar).

offshore edge (damping density to the initial state and velocities toward zero), and periodic boundary conditions in y . To track shelf water as it is transported offshore and downslope, a passive tracer is introduced. Its values are set to 1.0 at the surface in the forcing region and damped to zero within the offshore sponge boundary at every time step. In 2D, we perform a sensitivity analysis with doubled and quadrupled (both in x and z) resolutions, keeping the original viscosity values. Additionally, we explore a more realistic quadrupled-resolution case where the viscosity values are also decreased by a factor of 4 with explicit diffusivities.

The model begins from rest, with initial density stratification based on observations from the Kara and Barents Sea shelves without the Atlantic inflow layer (Rudels et al. 2000; Fig. 1b). Both salinity and temperature profiles are monotonic and stably stratified. All simulations feature a continental shelf that undergoes temporally constant negative buoyancy forcing at the surface (Fig. 1a), representative of the Arctic during the sea ice formation period (Cavaliere and Martin 1994). This forcing comprises an upward heat flux and downward salt flux representing the effects of brine rejection. The nominal value of the heat flux is 500 W m^{-2} , corresponding to a buoyancy forcing of approximately $-4.93 \times 10^{-6} \text{ kg m}^{-2} \text{ s}^{-1}$, and the salinity buoyancy forcing is approximately $-2.92 \times 10^{-5} \text{ kg m}^{-2} \text{ s}^{-1}$. Note the heightened role of salinity forcing in setting the density of seawater at low temperatures. Various values of forcing (1/8, 1/4, 1/2, 2, and 3 times the nominal heat and salt fluxes) are explored to test sensitivity of the dynamics to forcing magnitude. The buoyancy forcing in all cases extends for 15 km over the shelf and decays to zero over a 2-km distance over the shelfbreak; in 3D, forcing is constant alongshore. This forcing may

represent either a coastal polynya or shelf region experiencing seasonal ice growth.

3. Case 1: 2D, nonrotating

We first consider the simplest idealization of a dense shelf overflow: a nonrotating 2D system ($f = 0 \text{ s}^{-1}$) where SI and baroclinic instability cannot develop. This case will serve as a benchmark to identify the roles of rotation, SI, and baroclinic eddies in guiding Arctic shelf overflows.

a. Theory

Following initialization of buoyancy forcing at the surface of the forcing region, dense fluid will begin to convectively mix downward. We define the density anomaly in the forcing region $\Delta\rho$ as the average density of the entire water column within the forcing region at time t (where t is time following forcing initialization) minus the initial average density of the same region. As discussed by Gawarkiewicz and Chapman (1995), the density anomaly is initially expected to increase linearly as

$$\Delta\rho = Qt/H. \quad (2)$$

Here, Q is total buoyancy forcing with units ($\text{kg m}^{-2} \text{ s}^{-1}$), and H is water depth in the forcing region (40 m). As $\Delta\rho$ grows, the dense fluid will begin to move offshore and downslope. We can anticipate an eventual steady state of zero net buoyancy flux within the forcing region (of length $R = 15$ km), where the buoyancy flux imposed at the surface is balanced by offshore flow of dense water with some characteristic velocity U :

$$QR \sim \Delta\rho UH. \quad (3)$$

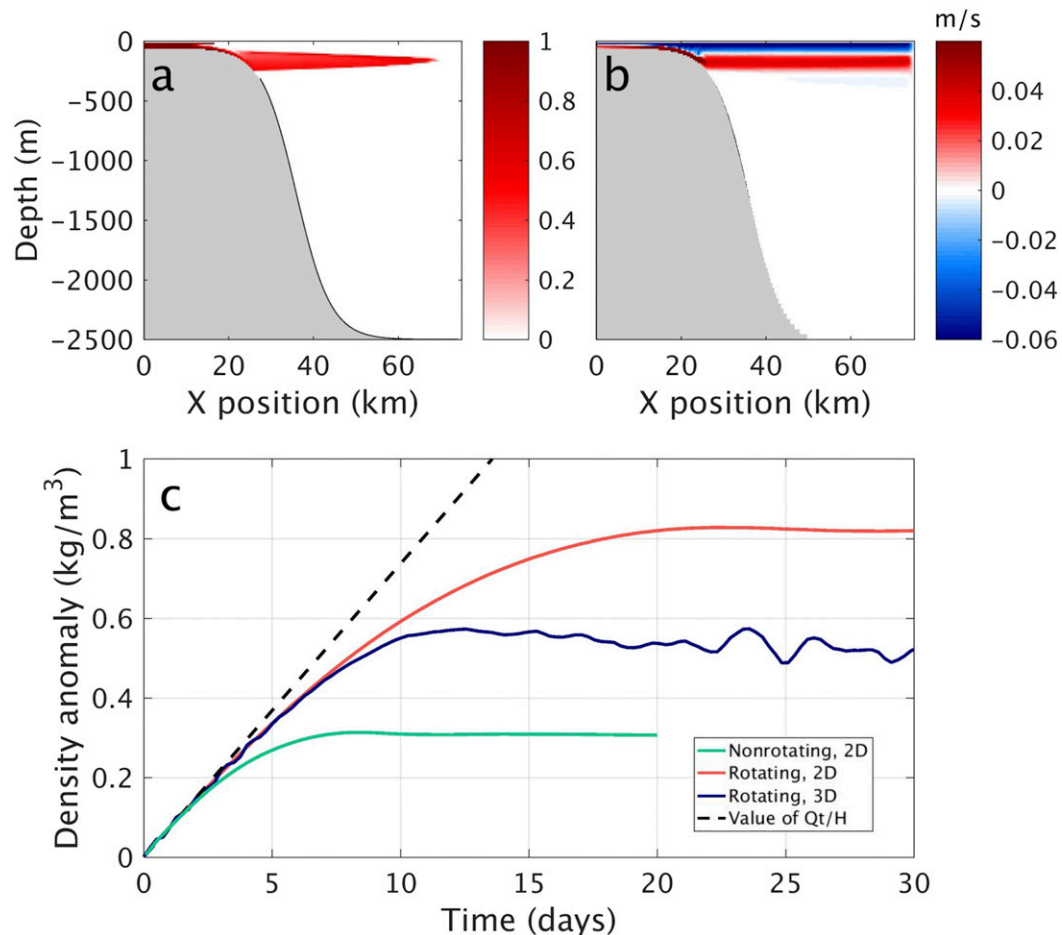


FIG. 2. For the nonrotating 2D case with nominal forcing at 20 days, (a) the depth cross section of passive tracer concentration and (b) offshore velocity u . (c) A comparison of forcing region density anomaly [Eq. (2)] as a function of time for the nonrotating and rotating cases (all with nominal forcing).

b. Results

We consider results from only the first 20 days of the simulations for the 2D nonrotating cases, as a steady state is achieved within 10 days. Figure 2c shows the density anomaly $\Delta\rho$ as a function of time for the nominal forcing case. As predicted, originally, the density anomaly within the forcing region grows linearly according to Eq. (2). The growth of $\Delta\rho$ slows as the gravitationally unstable dense water is advected offshore. A steady state is achieved after 8 days, where the density anomaly remains constant due to the balance between buoyancy forcing and offshore advection [Eq. (3)]. In Figs. 2a and 2b, the passive tracer concentration and offshore velocity are shown. The dynamics are relatively simple: the overflow propagates downslope as a gravity current until attaining a neutral buoyancy level with the surrounding water and then moving offshore. There is a compensating return flow

into the shelf region near the surface. The structure shown in Figs. 2a and 2b is maintained at steady state by the presence of the sponge boundary at the offshore edge. In Fig. 3a, we examine the sensitivity of these dynamics to the buoyancy forcing magnitude. The overflow is defined as water with a passive tracer concentration $\tau \geq 0.01$. The center of mass in the vertical $Z(x)$ is computed for overflow water at every point in the x direction (Legg et al. 2006):

$$Z(x) = \frac{\int \tau(x)z \, dz \, dy}{\int \tau(x) \, dz \, dy}. \quad (4)$$

This value is plotted for all of the buoyancy forcing cases (Fig. 3a). The equilibration depth is defined as the value of $Z(x)$ offshore from the shelf region. For all forcing cases, the equilibration depth remains relatively

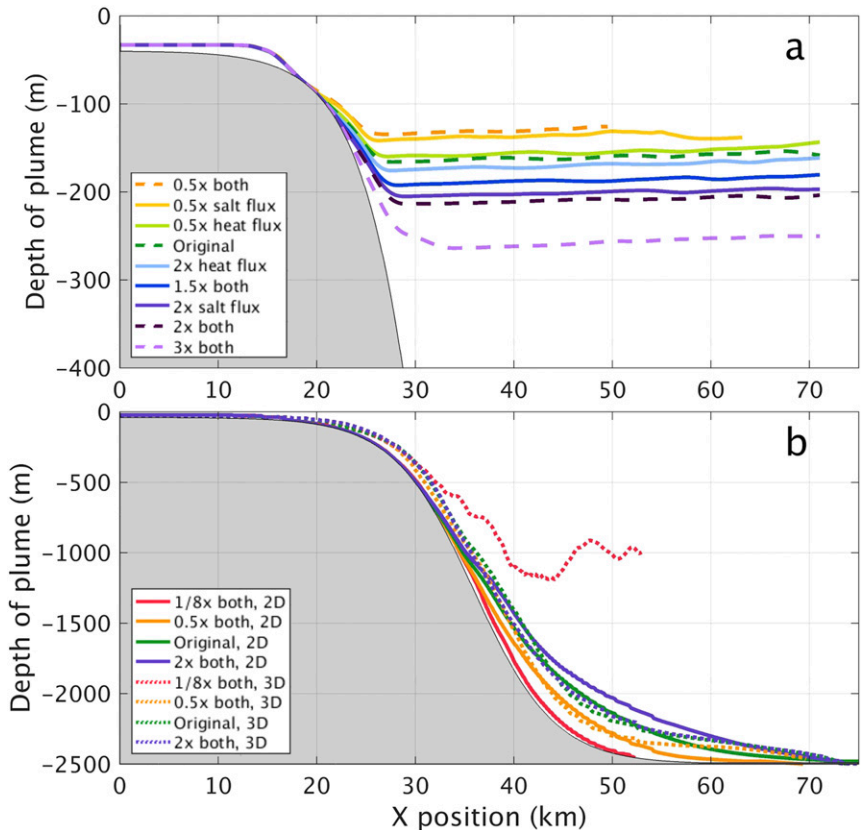


FIG. 3. Overflow center of mass in the vertical direction, as a function of offshore distance for a variety of buoyancy forcing values [Eq. (4)]. (a) The nonrotating 2D cases and (b) the rotating 2D and 3D cases.

shallow, within 300 m of the surface, even for the unrealistically strong 3x forcing case. Although these dynamics are capable of ventilating the uppermost layers and maintaining the Arctic halocline (depth of ~50–200 m), a different mechanism is clearly necessary to explain the presence of overflow water within the deepest portions of the Arctic.

4. Case 2: 2D, rotating

We now examine the effects of adding rotation to the 2D system described in the previous section. Fundamentally, this changes the problem so that dense shelf water is no longer free to propagate directly offshore and downslope. Rotation confines the shelf water laterally, causing it to remain in the forcing region longer and attain a greater density anomaly.

a. Theory

As in the nonrotating 2D case, we anticipate the density anomaly to initially grow as described by Eq. (2). Similarly, due to gravitational instability, the fluid will

begin to move downslope. In this case, however, rather than flowing offshore, the dense water will be deflected to the right by Earth’s rotation and will undergo geostrophic adjustment. The Coriolis force acts to steer the fluid upslope, confining it within the forcing region, while the pressure gradient forces the fluid downslope. This leads to predominantly along-isobath flow with an anticyclonic bottom-intensified geostrophic jet and compensating surface-intensified cyclonic jet (Gawarkiewicz and Chapman 1995).

In 2D, the dominant mechanism responsible for breaking geostrophy is bottom friction, imposed in the model through the prescribed viscosities and no-slip bottom boundary condition. Ekman dynamics in the bottom frictional layer has been found to play an important role in breaking geostrophic balance in the context of dense water overflows (Shapiro and Hill 1997). As described by Wirth (2009), the bottom frictional layer produces a leakage of dense water out of the geostrophic current, leading to downslope dense water transport through the frictional layer—a process termed Ekman draining. This draining also causes the

geostrophic jet to be shifted downslope (Manucharyan et al. 2014). Thus, we expect initial growth of the density anomaly as in the nonrotating case, followed by geostrophic adjustment broken by bottom Ekman dynamics. This will presumably lead to the bottom-intensified jet of dense shelf water moving downslope, establishing an alongslope front conducive to the onset and growth of symmetric instability.

b. 2D symmetric instability

Returning to the definition of Ertel potential vorticity (PV) in Eq. (1) and rewriting it for a 2D system, we obtain

$$q = \underbrace{\frac{g}{\rho_0} \left(\frac{\partial \rho}{\partial x} \frac{\partial v}{\partial z} \right)}_1 + \underbrace{\frac{-g}{\rho_0} \frac{\partial \rho}{\partial z} \left(\frac{\partial v}{\partial x} + f \right)}_2. \quad (5)$$

In the Northern Hemisphere, the criterion for SI is that $q < 0$. For stably stratified conditions, $\partial \rho / \partial z$ is negative, making term 2 generally positive (the absolute vorticity is nearly always positive due to f). Thus, in order for q to be negative, there are two primary options: term 2 takes a negative sign due to localized unstable stratification, or term 1 is negative and larger in magnitude than term 2. The latter case—when horizontal density gradients ($\partial \rho / \partial x$) and v velocity shear ($\partial v / \partial z$) yield a large and negative term 1—is the case of pure SI. The other case (negative term 2) is seen with gravitational instabilities or hybrid symmetric-gravitational instabilities; the balanced Richardson number $\text{Ri}_B = f^2 N^2 / |\nabla_H b|^2$ (where N is buoyancy frequency and ∇_H is the horizontal gradient operator) may be used to differentiate between these types (see Thomas et al. 2013).

As described by Holton (2004), an equivalent instability criterion is that isopycnals must be locally steeper than isolines of zonal angular momentum ($M = fx + v$) for SI to develop. If this is the case, then by definition, as we move along an isoline of ρ , angular momentum will be decreasing:

$$(\partial M / \partial x)_\rho < 0. \quad (6)$$

Then, multiplying Eq. (6) by $(-g/\rho_0)\partial \rho / \partial z$, we return to our original criterion that q as defined by Eq. (5) is negative for an unstable flow.

CONSERVATIVE FLUX FORM OF ERTEL PV

To identify how and where the negative Ertel PV leading to SI development is generated, we employ the conservative flux form of the Ertel PV equation as described by Marshall and Nurser (1992). We begin with the mass-weighted Ertel PV, as in Eq. (1):

$$q = \boldsymbol{\omega}_a \cdot \nabla b, \quad (7)$$

where absolute vorticity is $\boldsymbol{\omega}_a = f\hat{\mathbf{k}} + \nabla \wedge \mathbf{u}$. Following Pedlosky (1992), the rate of change of Ertel PV following a parcel is

$$\frac{Dq}{Dt} = \boldsymbol{\omega}_a \cdot \nabla \frac{Db}{Dt} + \nabla b \cdot (\nabla \wedge F). \quad (8)$$

Here, $D/Dt = (\partial/\partial t + \mathbf{u} \cdot \nabla)$, and F represents frictional forces given by

$$F = \nu_H \nabla_H^2 \mathbf{u} + \nu_Z \nabla_Z^2 \mathbf{u}. \quad (9)$$

Parameters ν_H and ν_Z are the horizontal and vertical viscosities, respectively; $\nabla_H^2 = \partial^2/\partial x^2|_z + \partial^2/\partial y^2|_z$ and $\nabla_Z^2 = \partial^2/\partial z^2|_{x,y}$ are the horizontal and vertical Laplace operators. We can then express Dq/Dt using a nonadvective flux (Marshall and Nurser 1992), after noting that vorticity is divergence free ($\nabla \cdot \boldsymbol{\omega}_a = 0$) and that the curl of a gradient is zero ($\nabla \wedge \nabla b = 0$):

$$\frac{Dq}{Dt} = \nabla \cdot \left(F \wedge \nabla b + \boldsymbol{\omega}_a \frac{Db}{Dt} \right). \quad (10)$$

The continuity equation then leads to the following conservative flux form of the Ertel PV equation, where rate of change of Ertel PV is the negative divergence of a flux vector \mathbf{J} :

$$\frac{\partial q}{\partial t} = -\nabla \cdot \left(\mathbf{u}q - F \wedge \nabla b - \boldsymbol{\omega}_a \frac{Db}{Dt} \right) = -\nabla \cdot \mathbf{J}, \quad \text{or} \quad (11)$$

$$\frac{\partial q}{\partial t} + \nabla \cdot \mathbf{J} = 0. \quad (12)$$

Considering a spatially fixed volume of fluid (such as a model grid box), the time rate of change of Ertel PV in this volume is therefore the sum of the convergence of the three terms of \mathbf{J} within the box. The first term ($\mathbf{u}q$) is the advection of Ertel PV into the box, the second term ($-F \wedge \nabla b$) is frictional generation/destruction of Ertel PV, and the last term ($-\boldsymbol{\omega}_a Db/Dt$) is the forcing contribution (the numerical diffusion component is not considered).

c. Results

Although two complete sets of resolutions were tested for the 2D rotating case (nominal and doubled), here, we present the doubled-resolution results. The dynamics were nearly identical, but SI is better resolved in this case. The sensitivity analysis and quadrupled-resolution case with lowered viscosity are presented in the next subsection. As anticipated, the density anomaly (Fig. 2c)

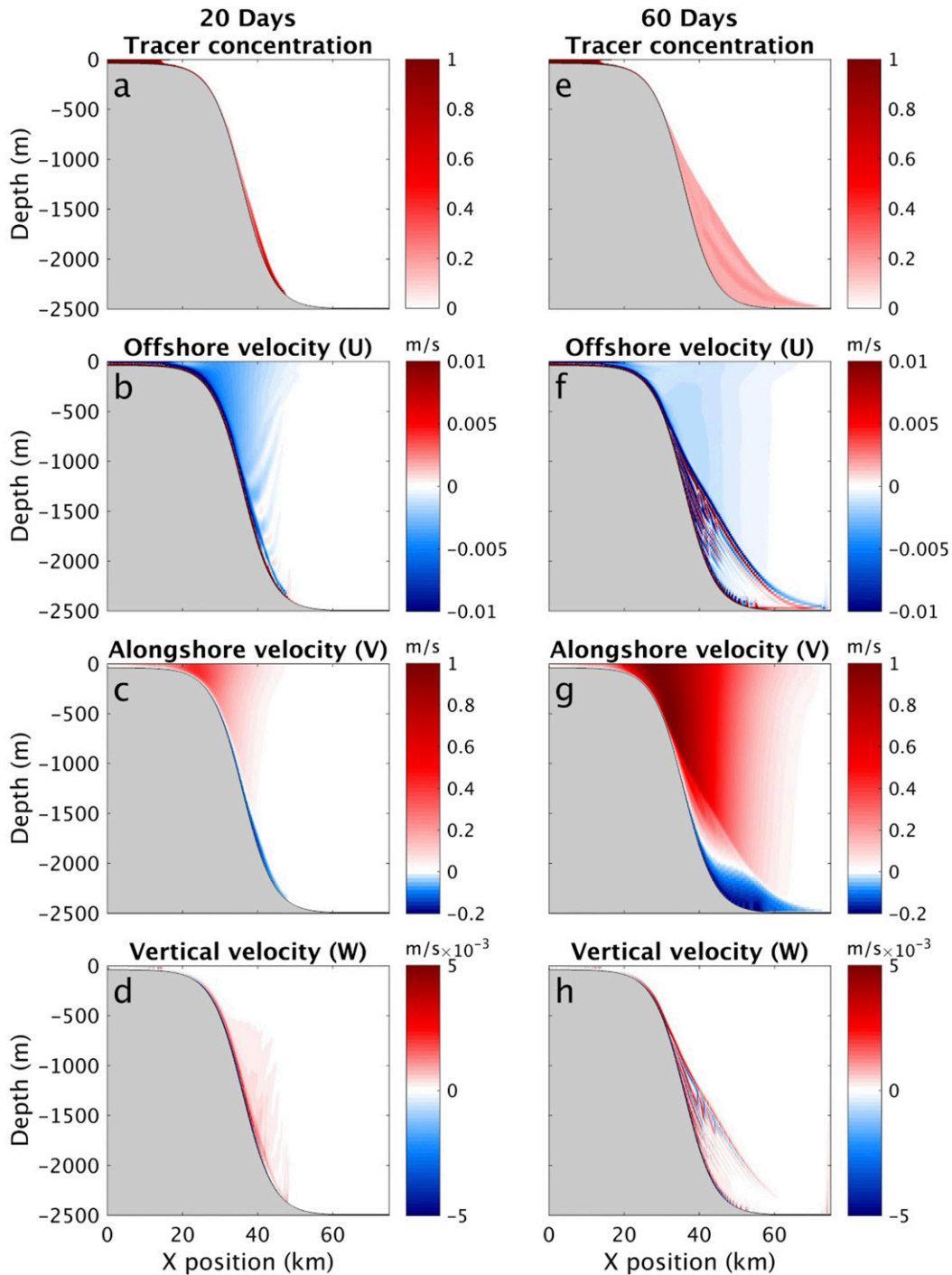


FIG. 4. For the rotating 2D case with nominal forcing, depth cross sections of tracer concentration and u , v , and w velocities at (a)–(d) 20 and (e)–(h) 60 days.

reaches values much higher than the nonrotating case (and even the 3D case due to the lack of advection by baroclinic eddies). This ultimately allows the overflow to propagate into the deepest portions of the domain (Fig. 3b). Figure 4 shows passive tracer distribution and

velocity fields at 20 and 60 days. The alongshore velocity component v is shown for these times, respectively, in Figs. 4c and 4g. The bottom-intensified jet is the negative velocity region (blue) at the bottom of/along the slope in both cases, while the surface-intensified jet is the

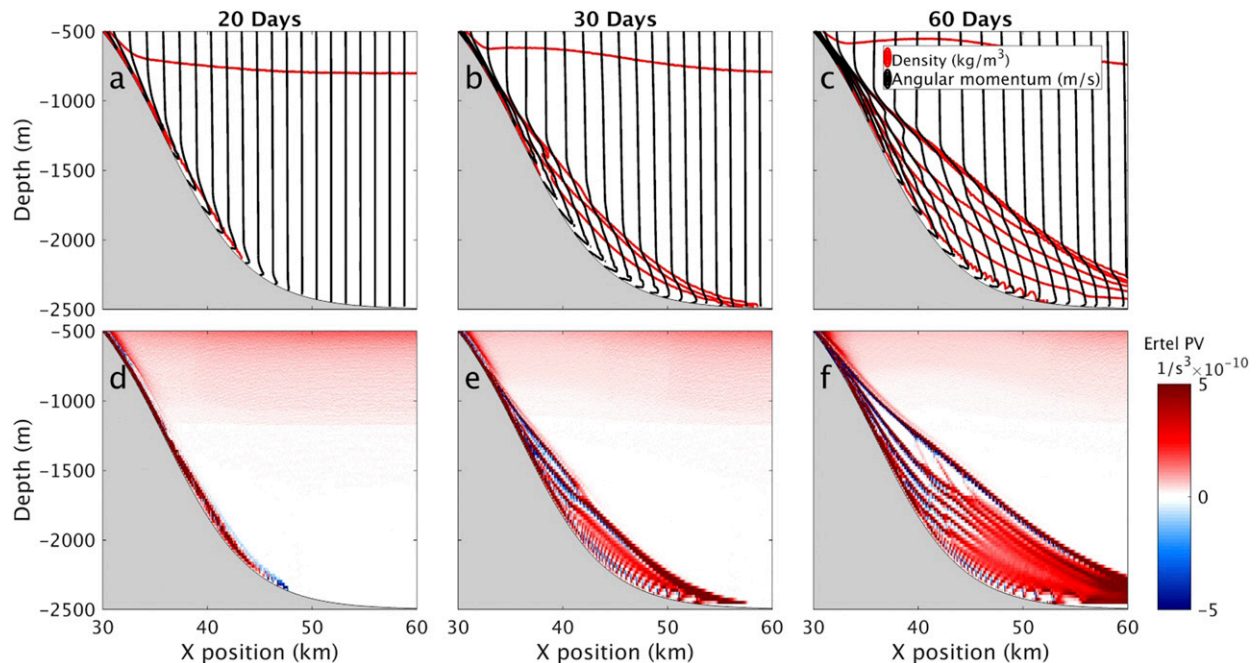


FIG. 5. (top) For the rotating 2D case with nominal forcing, depth cross sections of zonal angular momentum and density isolines at (a) 20, (b) 30, and (c) 60 days. (bottom) Depth cross sections of Ertel potential vorticity at (d) 20, (e) 30, and (f) 60 days.

positive velocity above. In this convention, negative (positive) velocity is directed out of (into) the page. The upper jet is much stronger; bottom friction damps the lower jet, while there is no surface drag acting on the upper jet.

As predicted, even by 20 days, bottom Ekman dynamics has caused the lower jet to be shifted nearly to the bottom of the slope. The tracer concentration plot at 20 days shows the thin layer of dense shelf water produced as a result of the bottom geostrophic jet leakage and descent. At 20 days, the presence of strong vertical shear in the alongshore velocity along with the sharp density front adjacent to the slope initiates SI. By 60 days, u and w velocity fields show diagonal velocity beams characteristic of SI; the resulting small-scale velocity gradients lead to viscous mixing. The gradient Richardson number ($Ri = N^2/|\partial u/\partial z|^2$) was calculated to test for presence of shear instabilities, but critical values ($0 < Ri < 0.25$) are found only in the bottom boundary layer. Secondary shear instabilities of SI are not captured at this resolution and viscosity, but do appear in the quadrupled-resolution case discussed below. SI-driven mixing is thus responsible for the offshore spreading of dense water as seen in the 20- and 60-day tracer fields (Figs. 4a,e).

The instability criteria are illustrated in Fig. 5. Figures 5a–c show isopycnals and isolines of zonal angular momentum M for 20, 30, and 60 days. As previously

shown in Fig. 4, at 20 days, a thin density front has developed along the slope, tilting the isopycnals upward from horizontal. On the other hand, the velocity field produced by the geostrophic current tilts the angular momentum isolines toward the horizontal, away from their initial vertical state. This creates near-slope regions where isopycnals are steeper, meeting the criterion for SI. SI then acts to flatten the steepened isopycnals, mixing water along the length of the overflow and pushing the density front offshore. However, the sharp density front is maintained by forcing and continues to generate SI moving away from the slope. This is visible in Figs. 5d–f, where the values of Ertel potential vorticity are shown at the corresponding times. At 20 days, a thin negative PV region is visible along the frontal edge (at $x \approx 47$ km), and at later times, there are negative beams both at the frontal edge and within the overflow (similar to the u and w velocity pattern shown in Fig. 4).

We examine the locations of negative Ertel PV again in Fig. 6 for days 20 and 60, this time isolating only negative values for better visualization. The two terms of Eq. (5) are plotted in Fig. 6 for 20 and 60 days. In Figs. 6d–f, where the instability is fully developed, we see that in regions of negative Ertel PV, term 1 must be negative and larger in magnitude than term 2 (pure SI). However, for the 20-day case, there is a region at the downgoing head of the overflow that is gravitationally

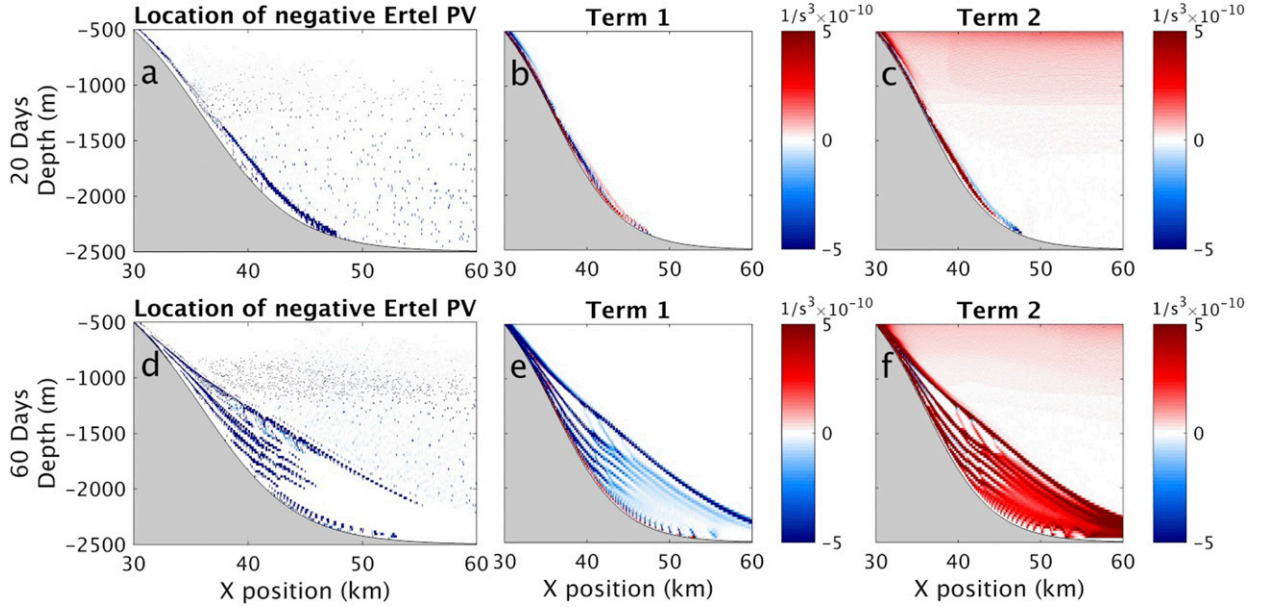


FIG. 6. Locations of negative Ertel PV and the two terms of the Ertel PV equation [Eq. (5)] for the rotating 2D case with nominal forcing at (a)–(c) 20 and (d)–(f) 60 days. Term 1 is $(g/\rho_0)[(\partial\rho/\partial x)(\partial v/\partial z)]$, and term 2 is $(-g/\rho_0)(\partial\rho/\partial z)[(\partial v/\partial x) + f]$.

unstable (negative term 2). Thus, the dense water initially flows down the slope as a gravitational instability driven by the Ekman dynamics of the geostrophic jet, and as the alongslope density front becomes established, pure SI develops.

Having identified the presence of SI, we turn to considering the processes responsible for generating the negative Ertel PV leading to its onset. In Fig. 7, we examine Ertel PV fluxes within each grid cell to understand how/where negative Ertel PV arises. The top panel shows Ertel PV values at 20 and 60 days (Figs. 7a,f). Below is the total time change of Ertel PV and the individual forcing, friction, and advection components at 20 and 60 days [see Eq. (11)]. Only the negative time changes are shown for the components—when all values are plotted, the beams of SI contain extremes of positive and negative values adjacent to each other (SI acts to homogenize Ertel PV), as is seen in the total time change plots (Figs. 7b,g). Clearly, forcing acts to inject negative Ertel PV at the surface—this is constant in time. At 20 days, when the overflow has established a density front along the slope (with water continuing to move downward along the slope), we see that friction is generating negative PV adjacent to the slope, extending up through the shelfbreak (Fig. 7d). The negative region of Ertel PV initiates SI at 20 days in a beam oriented along the slope/front, as seen in Figs. 4–6. SI then mixes water within this negative Ertel PV region, causing offshore advection of the overflow’s density front and negative PV beams (Figs. 7e,j).

Finally, we examine the effects that SI has on the kinetic energy distribution of the system. In Fig. 8, we plot velocity magnitudes comprising only the u and w components (Fig. 8b) and all three components (Fig. 8d). The former is dominated by the SI signature, while the latter is dominated by the geostrophic velocity. We consider a transect oriented perpendicular to the slope (direction of SI propagation) near the bottom; this line is shown in black. We then compute energy spectra along this line at various times (represented by different colors). At 5 and 10 days, the overflow has not yet reached the transect depth (energy values are relatively small). At 18 days, the overflow first reaches the location of the transect, and at 20 days, SI starts to develop in this region. The spectral characteristic of SI is clearly visible in Fig. 8a—the initial peak develops at a wavelength of approximately 300 m, with progressively smaller peaks developing with time down to the lowest resolvable wavelengths (40 m). In Fig. 8c, the v -velocity component dominates the signature, but nonetheless, some (noisier) peaks are evident below the 1000-m scale.

d. Sensitivity analysis

To examine the robustness of the observed 2D SI-driven dynamics, we perform a sensitivity study in which 1) the resolution is increased with viscosity kept constant, and 2) at the highest (quadrupled) resolution, the viscosity is made 4 times smaller so there is greater scale separation between the SI and viscous scales, and the

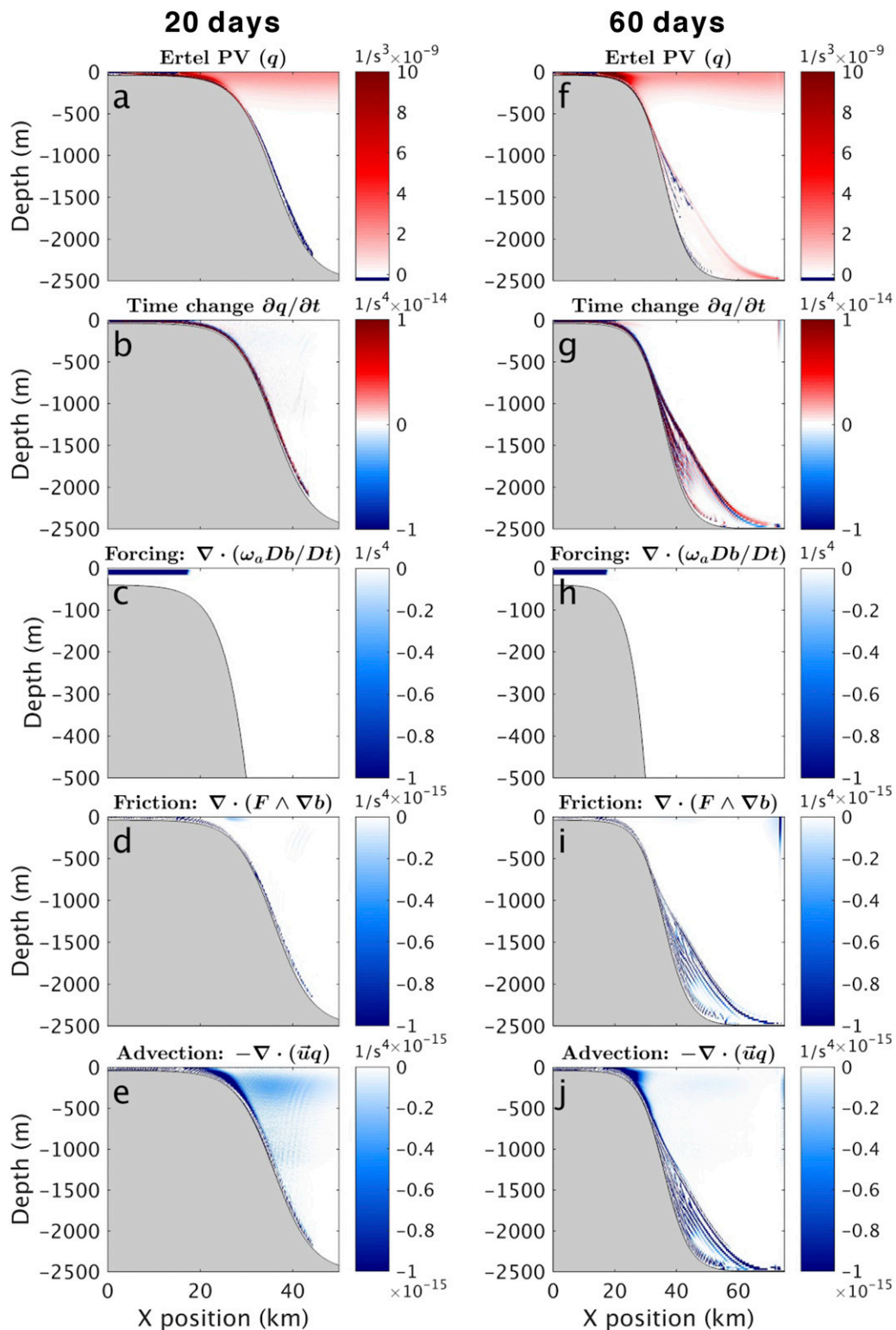


FIG. 7. (a) Ertel PV values for the rotating 2D case with nominal forcing averaged about a 2-day period centered at 20 days; (b) the likewise-averaged total time evolution of Ertel PV; (c)–(e) negative values of the flux components [Eq. (11)]. (f) Ertel PV values averaged near 60 days, with the (g)–(j) corresponding budget total and negative components.

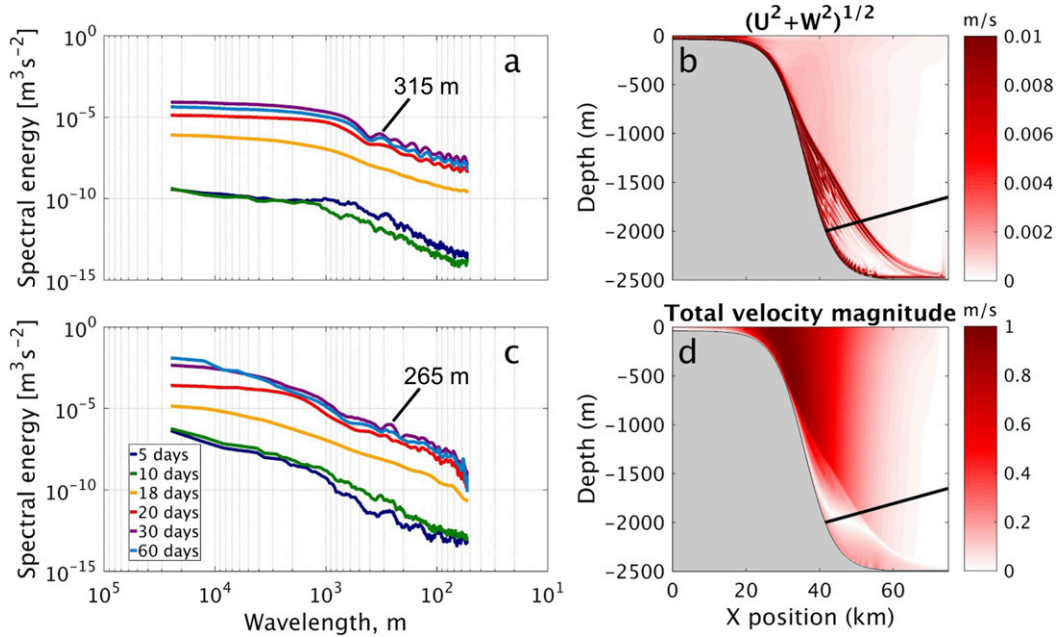


FIG. 8. For the rotating 2D case with nominal forcing, velocity magnitudes (b) without and (d) with the along-shore velocity component, and (a),(c) the corresponding spectra. Spectra are calculated at several times and are found along the black line oriented normal to the slope in (b),(d).

dynamics are more realistic. For the latter, temperature and salinity diffusivities of 1/1000 of the viscosity values are used (although a zero explicit diffusivity case was tested and found to have no appreciable difference). Figures 9a–c show locations of negative Ertel PV at constant viscosity for the original, doubled, and quadrupled resolutions. At the lowest resolution, the beams of SI appear pixelated, as the scale of the SI is near the grid size. As resolution increases, the SI becomes better resolved but unchanged in character. The same dynamics of tilted isopycnals and angular momentum isolines responsible for generating the SI are observed in Figs. 9e–g. Other metrics, including final density distribution and overflow depth, were also found to be unchanged, indicating numerical convergence of the results. Once viscosity is decreased in the quadrupled-resolution case (Figs. 9d,h), the dynamics acquire a previously uncaptured feature: secondary shear instability resulting from the strong velocity gradients set up by the SI. Figure 10 shows a close-up view of the region where SI and its secondary shear instabilities develop. The velocity beams and regions of negative PV do not follow such clean patterns as the higher viscosity case due to the initiation of shear instability between SI beams. This is evident in the gradient Richardson number taking critical values between beams of SI (Figs. 10c,g) and the noisier signature and rollups of the isopycnals

(Figs. 10d,h). The final density distribution was nonetheless found to be nearly identical to the higher viscosity case. Another test was performed in which the temperature and salinity diffusivities were set equal to the viscosity values, suppressing overturning instabilities potentially arising in nonunity Prandtl number flows (McIntyre 1970). In this case, the heightened diffusivity values lead to erosion of the density gradients within the overflow, allowing the critical Richardson number criterion to be even more easily satisfied. Still, analogous dynamics are observed, with SI developing within the overflow and shear instabilities initiated between SI beams. Thus, SI is shown to be a robust mechanism for initiating mixing—either in the form of direct viscous dissipation (lower resolution) or secondary shear instability leading to viscous dissipation (higher resolution).

5. Case 3: 3D, rotating

We now examine the effects of adding an along-shore dimension to the 2D rotating system described in the previous section. The width of the y domain is 100 km, much greater than the baroclinic Rossby deformation radius ($L_R \approx 5$ km). Whereas in the 2D rotating case, bottom friction is the dominant mechanism breaking geostrophy, baroclinic eddies now become possible.

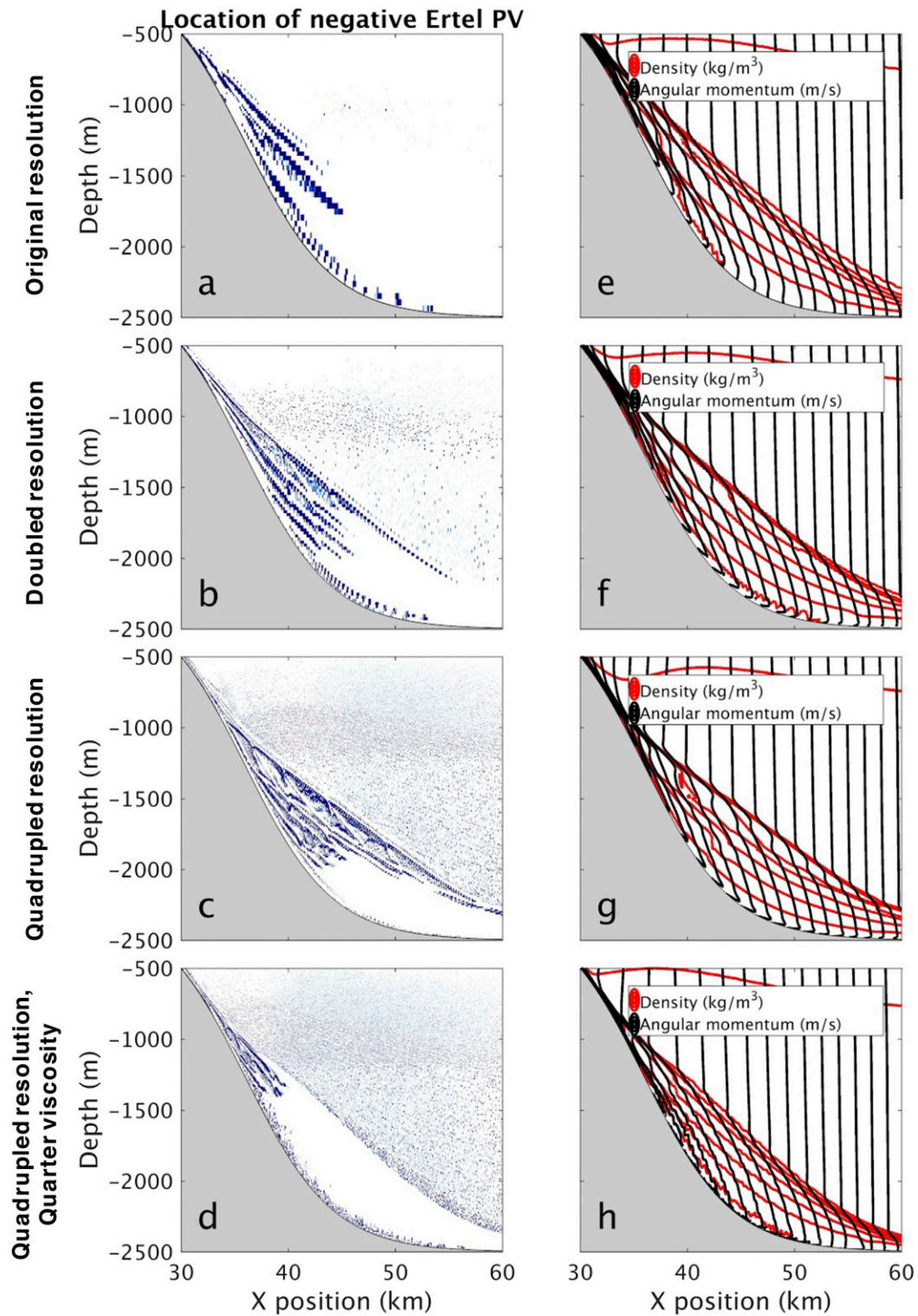


FIG. 9. Sensitivity analysis for the rotating 2D case with nominal forcing. (a)–(c) Locations of negative Ertel PV at 60 days for the original, doubled, and quadrupled resolution cases with the original viscosity values ($\nu_H = 2.5 \text{ m}^2 \text{ s}^{-1}$ and $\nu_Z = 0.01 \text{ m}^2 \text{ s}^{-1}$). (e)–(g) Corresponding plots of isopycnals and angular momentum isolines. (d), (h) The same quantities for the quadrupled-resolution case with 4 times smaller viscosity values and explicit temperature and salinity diffusivities (set to 1/1000 of the viscosity values).

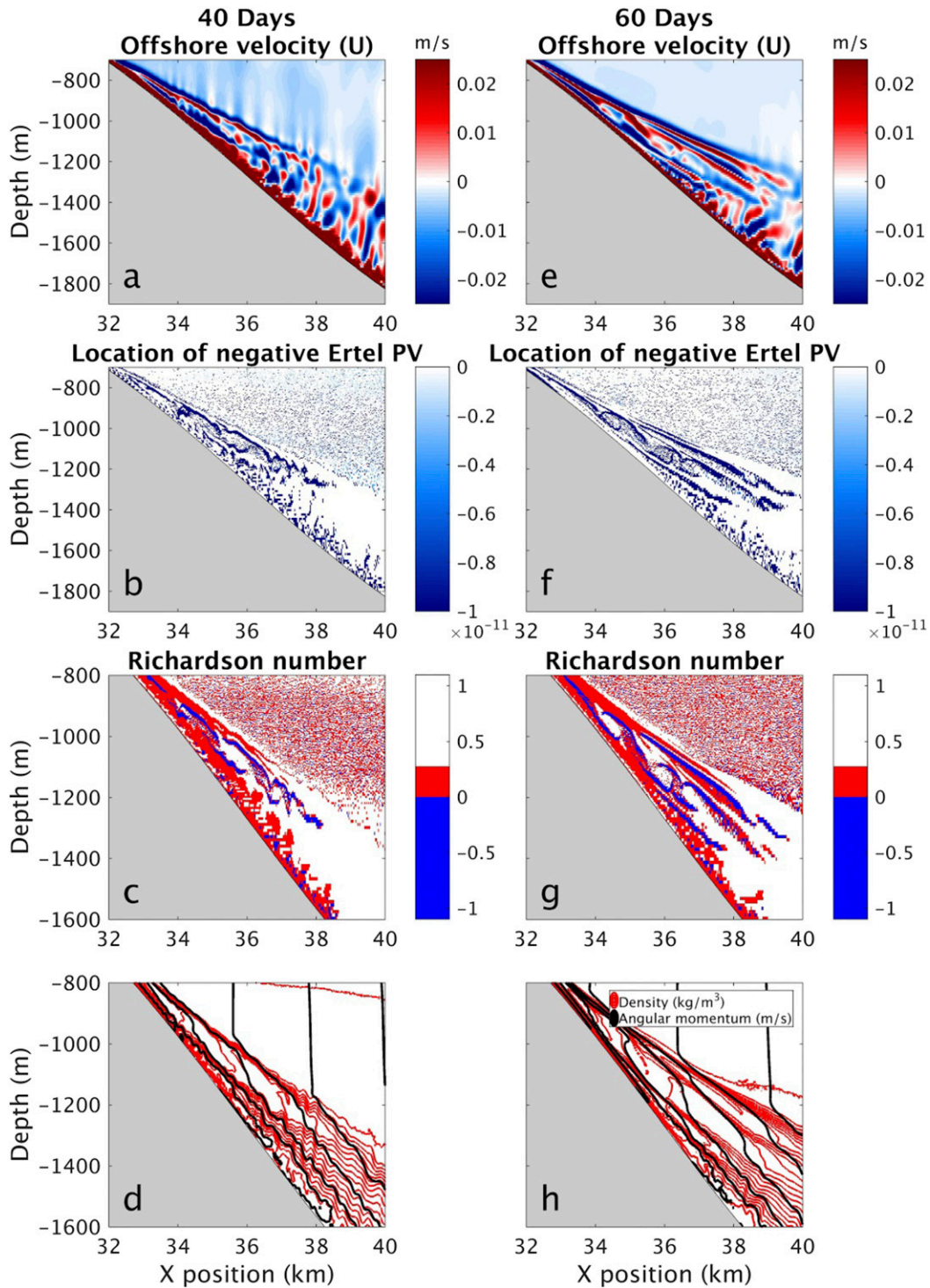


FIG. 10. For the quadrupled-resolution case with viscosities set to 1/4 of the nominal values and explicit diffusivities (1/1000 of viscosity values): (a) u velocity, (b) locations of negative Ertel PV, (c) Richardson number with critical values shaded in red, and (d) angular momentum and density isolines at 40 days. (e)–(h) As in (a)–(d), but at 60 days.

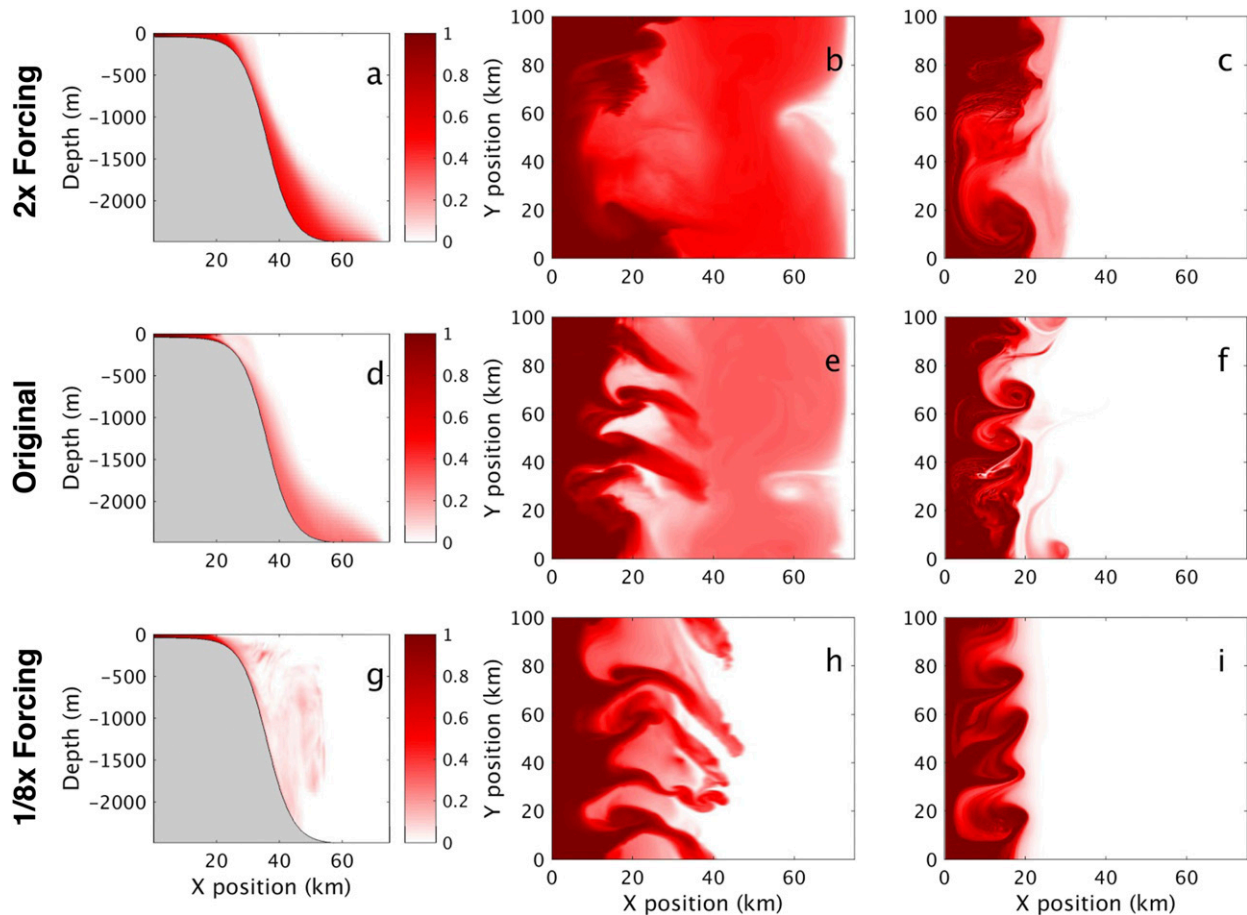


FIG. 11. For the rotating 3D case with doubled forcing at 60 days: (a) alongshore-averaged tracer concentrations, (b) tracer values at the lowest grid point everywhere in the domain, and (c) tracer values near the surface (at depth 20 m). The same quantities as in (a)–(c), but for the (d)–(f) nominal forcing case at 60 days and (g)–(i) 1/8 forcing case at 120 days.

a. Theory

As before, we anticipate the density anomaly in the forcing region will initially grow as described by Eq. (2), the gravitationally unstable fluid will begin to move offshore/downslope, and geostrophic adjustment will occur. Unlike the 2D rotating case, however, baroclinic eddies are now free to develop in the alongshore direction. Such a case was previously studied by Gawarkiewicz and Chapman (1995), using a coarser-resolution hydrostatic model. They described these overflow dynamics in terms of three phases: geostrophic adjustment; development of baroclinic instability; and rapid offshore, cross-isobath eddy transport of dense water. The forcing used in their study was similar to our nominal forcing case, and the dense water was found to make its way into the deepest portions of the domain—a mechanism for ventilation of the abyssal Arctic. We test whether these dynamics hold for several forcing values and examine whether the density fronts formed by the

baroclinic eddies as they descend along the slope are capable of generating SI.

b. Results

Here, we consider results from the nominal buoyancy forcing as well as 1/8 and 2 times nominal forcing cases. For nominal forcing, the dynamics described by Gawarkiewicz and Chapman (1995) hold. Initially, the density anomaly grows as in Eq. (2) (Fig. 2c). There is a geostrophic adjustment phase and onset of baroclinic instability; eddies begin to develop within the shelf region around 5 days, growing in alongshore wavelength until about 20–30 days (longer for 1/8 forcing). This is evident in the plots of near-surface tracer concentration at quasi-steady state (Figs. 11c,f,i). When the edge of an eddy extends over the shelfbreak, dense fluid cascades along the slope into the deepest portions of the domain. This is illustrated in Figs. 11b, 11e, and 11h by plotting the tracer concentration at the lowest point everywhere

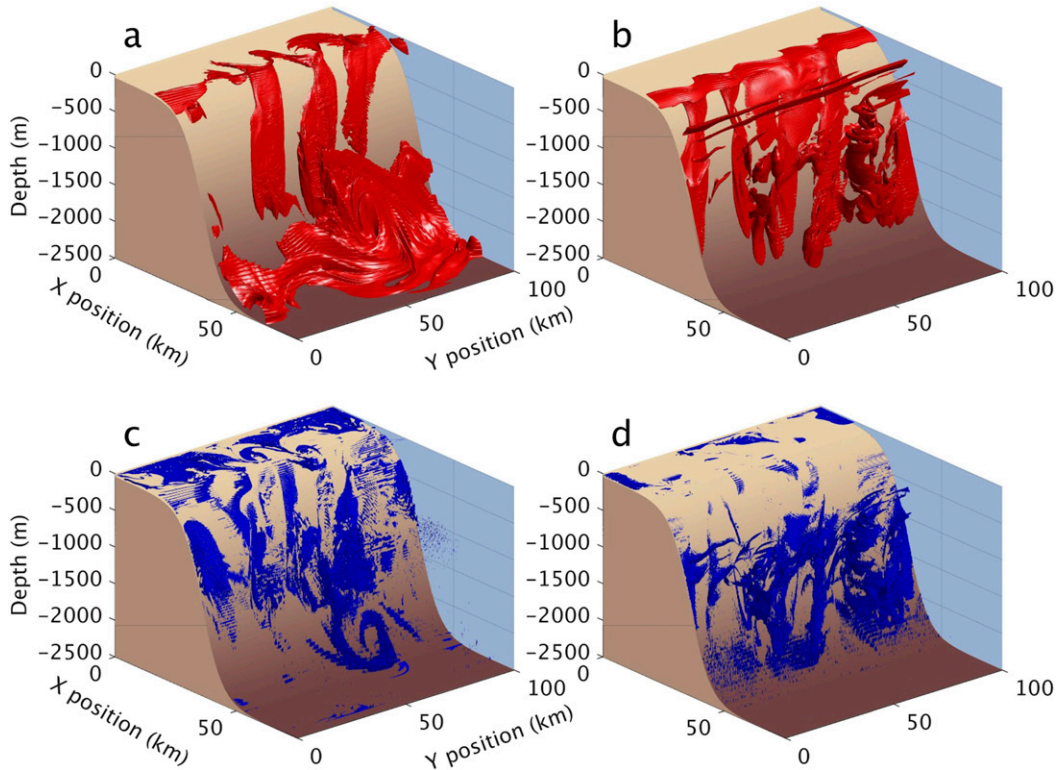


FIG. 12. Isosurfaces where tracer concentration is 0.3: (a) the nominal forcing case at 60 days and (b) the 1/8 forcing case at 120 days. (c),(d) The corresponding isosurfaces of negative Ertel PV.

in the domain. Particularly for the nominal and double forcing cases, topographically confined baroclinic eddies produce strong cross-isobath dense water transport down to 2500-m depth. For these two cases, the abyssal portion of the domain ($x = 40\text{--}75$ km, $z \leq -2000$ m) has high concentrations of passive tracer as a result (also shown in Fig. 3b). Note that among the bottom-confined cases in Fig. 3b, greater forcing magnitude leads to a slightly shallower center of mass; this is due to increased mixing and entrainment.

The first column of Fig. 11 shows alongslope-averaged passive tracer concentration. For the nominal and double forcing cases, again tracer is clearly present in the greatest depths and is mostly confined to the topography—eddies do not propagate into the interior but remain bottom trapped, as seen by Gawarkiewicz and Chapman (1995). However, for the 1/8 forcing case, the water within the eddies is less dense, and as a result, eddies are not bottom confined. Rather, they preserve their 3D structure and propagate into intermediate offshore depths as they equilibrate (Fig. 3b). This explains why there is so little tracer in the abyssal region of the 1/8 forcing case (Fig. 11h). Thus, forcing conditions consistent with strong atmospheric cooling and initial formation of sea ice may produce baroclinic eddies that are

confined to the topography and descend into abyssal depths. Weaker forcing cases, such as regions covered by young sea ice still releasing brine, may contribute to intermediate layer ventilation and halocline maintenance.

We see that baroclinic eddies in nominal/stronger forcing cases lead to highly dense water being confined along the slope, similar to the 2D rotating case. Since in the 3D cases there too is geostrophic shear and substantial horizontal density gradients, there is the potential for SI to develop. In Figs. 12a and 12b, the 0.3 isosurface of passive tracer concentration is plotted for the nominal and 1/8 forcing cases at quasi-steady state. This differentiates the character of the baroclinic eddies between the two cases (bottom confined vs intermediate). The alongslope density front is well defined for the nominal forcing case, while for the 1/8 forcing case, there are also density fronts that are produced along the edges of the 3D baroclinic eddies. Recalling the criterion for SI ($q < 0$), we plot the corresponding regions of negative Ertel PV in the panels below (Figs. 12c,d). Interestingly, in both cases, there are well-defined symmetrically unstable regions created along the density fronts (corresponding to the tracer isosurfaces).

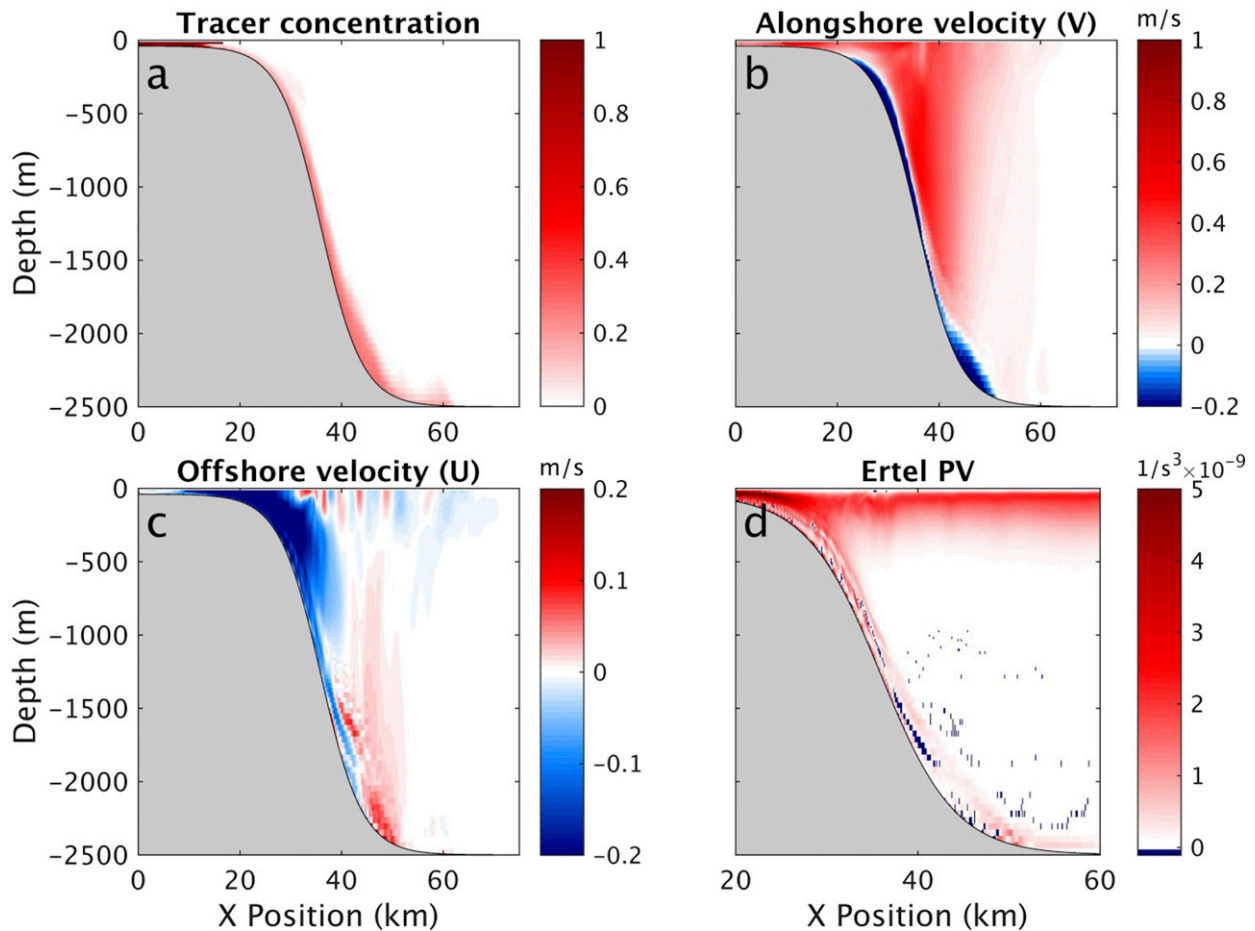


FIG. 13. Depth cross sections at $y = 50$ km for the rotating 3D case with nominal forcing at 30 days: (a) tracer concentration, (b) alongshore velocity, (c) offshore velocity, and (d) Ertel PV.

In Fig. 13, we examine depth cross sections of tracer concentration, velocity, and Ertel PV along an x - z transect. Even with the presence of baroclinic eddies, these results are qualitatively similar to the rotating 2D SI-dominated case (Figs. 13a,b). The u velocity field shows an alternating positive/negative pattern near the slope, and there is a beam of negative Ertel PV parallel to the slope (Figs. 13c,d). To further test for the presence of SI, we plot energy versus wavelength spectra to see whether a signature similar to the 2D SI-dominated case is observed. Spectra are calculated for the same transect shown in Fig. 8 (2D case), but extending in the y direction, thus forming a plane. Velocity fields (u , v , w , and velocity magnitude) within this plane and their corresponding spectra are shown in Fig. 14. The u velocity field is dominated by the periodic signature of the baroclinic eddies. The maximum energy is found at ~ 24 -km wavelength, corresponding to the average alongshore eddy wavelength. The predominantly geostrophic velocity field v has a bottom-intensified jet adjacent to the

slope and compensating surface-intensified jet. The total velocity field is dominated by the signature of the v velocity component. However, examining the w velocity field and spectrum, there are three noticeable peaks (Fig. 14e). One is again at 24 km, and the others are at 150 and 500 m, similar to the SI peaks in the 2D rotating case. This provides further proof that although the 3D case is dominated by mesoscale baroclinic eddies, SI is prevalent at submesoscales. Although further work is necessary to isolate the relative roles of each, we begin to address this question in the following discussion section.

6. Discussion

In this section, we apply several metrics to compare the two rotating regimes: 2D SI-driven and 3D baroclinic eddy-driven at the nominal buoyancy forcing magnitude. We begin by addressing how the density distribution changes in each case. We then calculate an

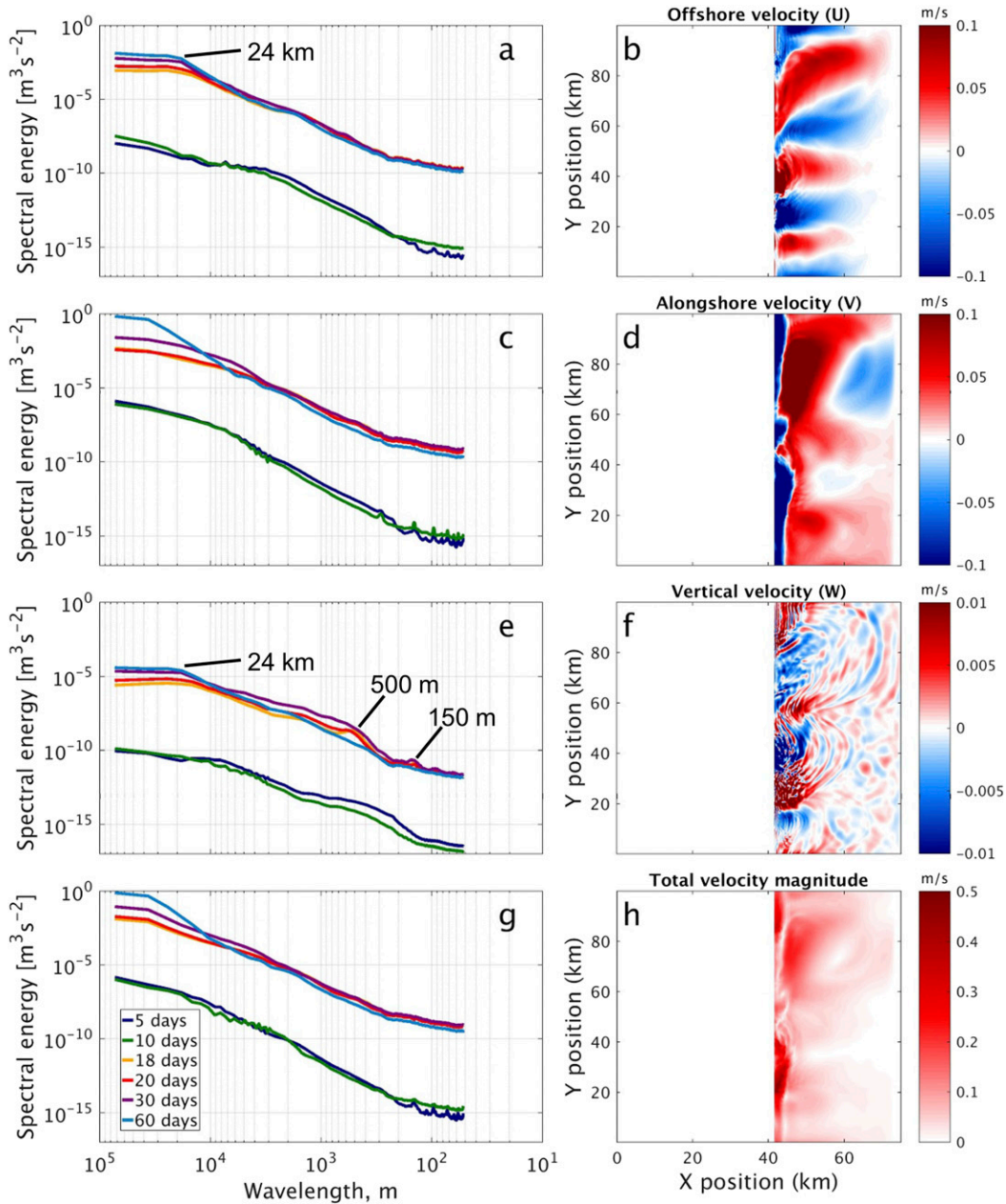


FIG. 14. For the rotating 3D case with nominal forcing, (b),(d),(f),(h) various velocity components and (a),(c),(e),(g) their corresponding spectra. Spectra are calculated in the plane formed by the black line shown in Fig. 8 that extends in the alongshore direction.

entrainment coefficient as defined by Turner (1986), following the implementation of Legg et al. (2006). Finally, we compare kinetic energy budgets for the two systems, similarly to the analysis by Brink (2017).

a. Water mass conversion

Here, we consider how the density distribution of water within the $x = 20\text{--}55\text{-km}$ region (overlying the continental slope) changes in time for the 2D and 3D

rotating cases. We examine the quasi-steady-state 30–60-day period, when SI and baroclinic eddies are well developed. First, the time change of volume (normalized by the total region volume) for each density class is computed. This is plotted in the top panels of Fig. 15 for the 2D case (Fig. 15a) and 3D case (Fig. 15b). Positive (negative) values indicate an increase (decrease) in volume at a given density class. The 30–60-day time change in density distribution for the two cases looks

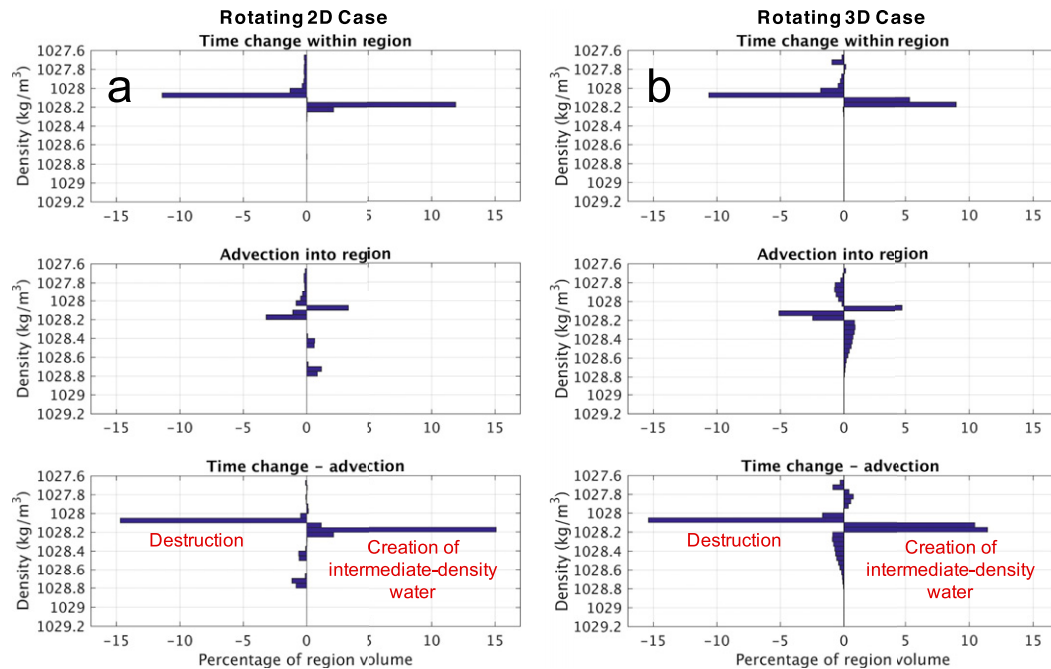


FIG. 15. Water mass conversion at nominal forcing: (a) rotating 2D SI-dominated case and (b) rotating 3D eddy-dominated case. Values are integrated over the 30–60-day period for the slope region (20–55 km in x). In each panel, the total volume of water within each density bin is computed and then divided by the volume of the region. (top) The time change of density distribution within the region, (middle) the distribution of net advected water into the region (positive indicates advection into the region), and (bottom) the difference (positive indicates creation).

quite similar: there is an increase of higher-density water and a decrease of lower-density water. Roughly the same percentage of the region volume and at the same density classes is changed.

Next, we examine the changes in density distribution from advection into the region (middle panel in Figs. 15a,b). Again, the two cases look quite similar, although the 2D results appear more discrete due to lack of along-slope averaging. If no mixing occurred within the region (no internal density changes), then the advected change in density distribution should equal the time change of density distribution within the region. Thus, subtracting advective change from time change gives an indication of which density classes were destroyed and created through mixing. This is done in the lowest panel of Fig. 15. Positive values indicate creation of water within a given density class through mixing; negative values indicate destruction. In both cases, there is destruction of more extreme density classes (very light and very dense) to create intermediate-density fluid.

Remarkably, even though the dynamics of the 2D and 3D cases are quite different, the resulting mixing creates and destroys water at the same density levels with approximately the same percentage of water by volume being modified. Further, we constructed analogous

histograms for the 1/8, 1/2, and double forcing cases and found similarity between the 2D and 3D cases. Water mass modification is a strong function of forcing, but 2D and 3D cases are very similar at a given forcing. The histograms for the 1/8 forcing case are shown in Fig. 16 (the 90–120-day period is used because eddies take longer to develop). This case is particularly interesting; recalling Fig. 3, the overflow center of mass is different for the 2D and 3D cases because the 3D eddies are not bottom confined, although the densest water still cascades along the slope (Figs. 11, 12). The water that intrudes into the interior is at its neutral buoyancy level and therefore does not result in any changes in density distribution. The strongest water mass modification occurs from nonequibrated dense water adjacent to the slope entering the domain (this is also where SI develops in both 2D and 3D). As a result, the 2D and 3D histogram results are once again nearly the same. Thus, the 2D case where the overflow descends through bottom Ekman dynamics and then is mixed offshore by SI, and the 3D case where baroclinic eddies are responsible for cascading water downslope, result in approximately the same final water mass distributions at a given forcing. This is encouraging for parameterization efforts; when a certain transport mechanism (e.g., baroclinic eddies) is

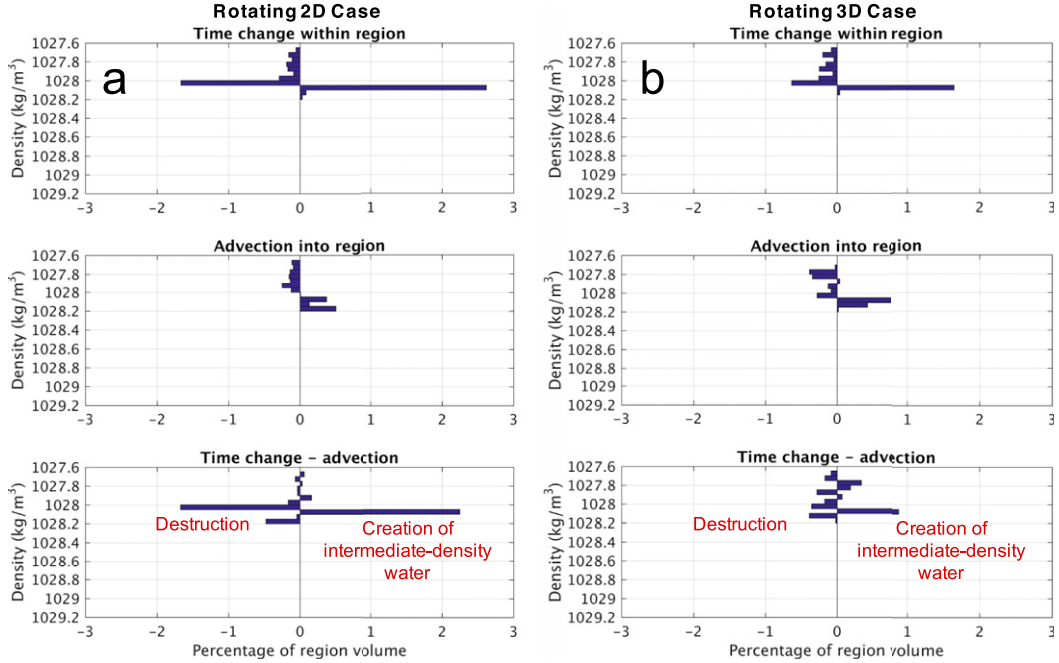


FIG. 16. Water mass conversion for 1/8 forcing: (a) rotating 2D SI-dominated case and (b) rotating 3D eddy-dominated case. Values are integrated over the 90–120-day period for the slope region (20–55 km in x). (Same quantities as Fig. 15.)

suppressed, the inherently unstable density distribution leads to a stable final state that is invariant to the particular mixing pathway.

b. Entrainment coefficient comparison

We next compare the entrainment coefficient as formulated by Legg et al. (2006) for the 2D SI-dominated and 3D baroclinic eddy-dominated cases. The overflow water is considered to be all water having a passive tracer concentration $\tau \geq 0.01$, covering cross-sectional area A . The offshore transport as a function of x [$T(x)$] of dense water by the overflow is defined as

$$T(x) = \int_A u \, dy \, dz, \quad (13)$$

where u is offshore velocity as before. The entrainment coefficient α_E is then

$$\alpha_E(x) = \frac{d}{dx} \frac{T(x)}{L\bar{u}}, \quad (14)$$

where L is the length of the interface between the overflow and ambient water in the offshore direction, and $\bar{u} = (1/A) \int_A u \, dy \, dz$ is the average offshore velocity within the overflow.

The entrainment coefficient as a function of x is plotted in Fig. 17 for the nonrotating 2D case, the

rotating 2D case, and the rotating 3D case (all at the same forcing values). In addition, the 1/8 forcing case in 3D is shown as a dotted black line. From this figure, it is evident that the magnitudes of entrainment in the 3D cases are significantly larger than the 2D cases. In 2D, the nonrotating and rotating cases have roughly the same, near-zero entrainment coefficient values. The 2D nonrotating results may be explained by cessation of the entrainment when the plume's neutral buoyancy is reached. In the 2D rotating case, there is clearly still mixing in spite of the small entrainment coefficient values (as shown earlier, there is a roughly equal amount of water mass conversion through mixing in the 2D SI-driven case and the 3D eddying case). As seen in the velocity field (Fig. 4), SI-driven mixing gives rise to both up- and downslope motion. However, this mixing is aligned with the topography and therefore does not increase in the offshore direction. Once baroclinic eddies are permissible in 3D, entrainment coefficient values become much larger (with the exception of the negative values, produced as the eddies reach the bottom and their offshore transport lessens). As discussed in the next section, kinetic energy is being continuously supplied to the growing eddies. Although the eddy-driven transport is adiabatic, eddies create vigorous stirring and initiate SI and mixing offshore, leading to high entrainment coefficient values.

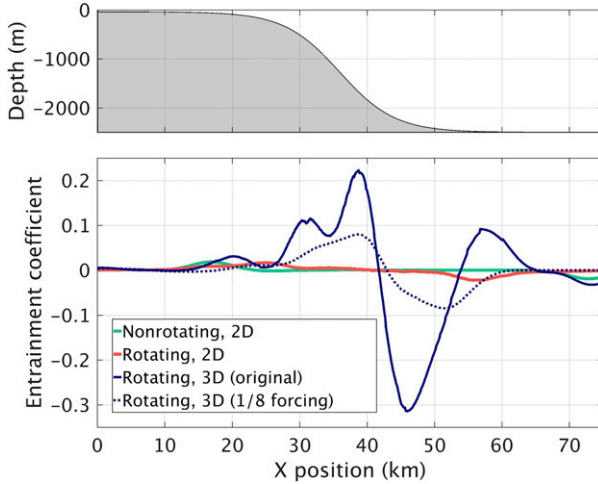


FIG. 17. Entrainment coefficient $\alpha_E(x) = [(d/dx)T(x)]/L\bar{u}$ (Legg et al. 2006) plotted as a function of offshore distance for the three model configurations at nominal forcing, as well as the 3D case with 1/8 forcing.

c. Energetics

Neglecting the viscous transport term (here, negligible when alongshore averaged), the kinetic energy budget for a Boussinesq fluid may be written as

$$\begin{aligned} \frac{\partial}{\partial t}(\text{KE}) = & -\nabla \cdot (\mathbf{u}\text{KE}) - \nabla \cdot (\mathbf{u}P/\rho_0) \\ & - \nu_H \left[\left(\frac{\partial \mathbf{u}}{\partial x} \right)^2 + \left(\frac{\partial \mathbf{u}}{\partial y} \right)^2 \right] - \nu_Z \left(\frac{\partial \mathbf{u}}{\partial z} \right)^2 + wb, \end{aligned} \quad (15)$$

where $\text{KE} = (1/2)(u^2 + v^2 + w^2)$, P is pressure, ν_H and ν_Z are the horizontal and vertical viscosities, and w is vertical velocity. We calculate each term in Eq. (15) and alongshore average and integrate in z for each dx slice to obtain energetics as a function of offshore distance x .

Thus, the temporal change of kinetic energy (KE) is given by the sum of an advective and pressure flux, conversion of KE to dissipation (DISS) by viscosity, and conversion of potential energy (PE) to KE. The latter two are the creation and destruction terms, with integral forms as follows:

$$C_{\text{PE} \rightarrow \text{KE}} = \frac{1}{A} \int_0^L \int_{-H}^0 \overline{(wb)} dz dx, \quad (16)$$

$$\begin{aligned} C_{\text{KE} \rightarrow \text{DISS}} &= \frac{-1}{A} \int_0^L \int_{-H}^0 \nu_H \left[\left(\frac{\partial \mathbf{u}}{\partial x} \right)^2 + \left(\frac{\partial \mathbf{u}}{\partial y} \right)^2 \right] + \nu_Z \left(\frac{\partial \mathbf{u}}{\partial z} \right)^2 dz dx. \end{aligned} \quad (17)$$

Here, an overbar denotes alongslope averaging; A is fluid area in the xz plane of length L and height H over which the conversion is computed. We calculate the terms given by Eqs. (16) and (17) and the other likewise-integrated terms of Eq. (15) for each grid column of length dx . Additionally, we calculate the residual between the time change and the right-hand side of Eq. (15). These results are plotted in Fig. 18 for the 2D rotating case (Fig. 18a) and 3D rotating case (Fig. 18b); corresponding topography is shown in the top panel, 10-day results are the middle panel, and 60-day results are below. The terms are averaged in time over 2.5 days to obtain a less noisy representation of the energetics.

At 10 days, baroclinic and symmetric instabilities in the two cases have not yet fully developed, but geostrophic adjustment has commenced. There are high values of PE to KE conversion in the shelf region in both cases, caused by the convective descent of the dense water from the forcing region and formation of the geostrophic jets. The conversion of KE to DISS has a well-defined peak in both cases around 13 km in x , corresponding to the location of the surface-intensified geostrophic jet and resulting shear. Overall, the two cases appear similar due to the lack of developed SI and eddies at 10 days.

When considering the 60-day plots, differences between the two cases emerge. The PE to KE conversion plot is still similar between the two, with a peak produced by the surface-intensified geostrophic jet around 25 km. However, for the 2D SI-dominated case, the conversion of KE to DISS follows the curve for the conversion of PE to KE very closely; the flux and time change terms are very small. This is not at all the case for the 3D baroclinic-eddy-driven case; here, the conversion of KE to DISS is much smaller in magnitude than the conversion of PE to KE. In other words, the potential energy is being used to feed the baroclinic eddies that are still growing (even at 60 days); kinetic energy of the system is being increased, as is evident from the positive time change term. The difference in KE dissipation highlights the contrasting mixing pathways of the 2D and 3D cases. The growing KE of the mesoscale eddies leads to increased stirring and volume entrainment moving offshore. In 2D, mixing primarily occurs by submesoscale alongslope SI acting to efficiently dissipate the kinetic energy of the geostrophic jet.

d. Relevance of results to the real ocean

Though the simulations presented in this work are idealized process studies, the results are relevant to numerous real-world flows. As stated previously, initial conditions and forcing values are based on observations obtained in the Kara and Barents Seas. Coastal regions

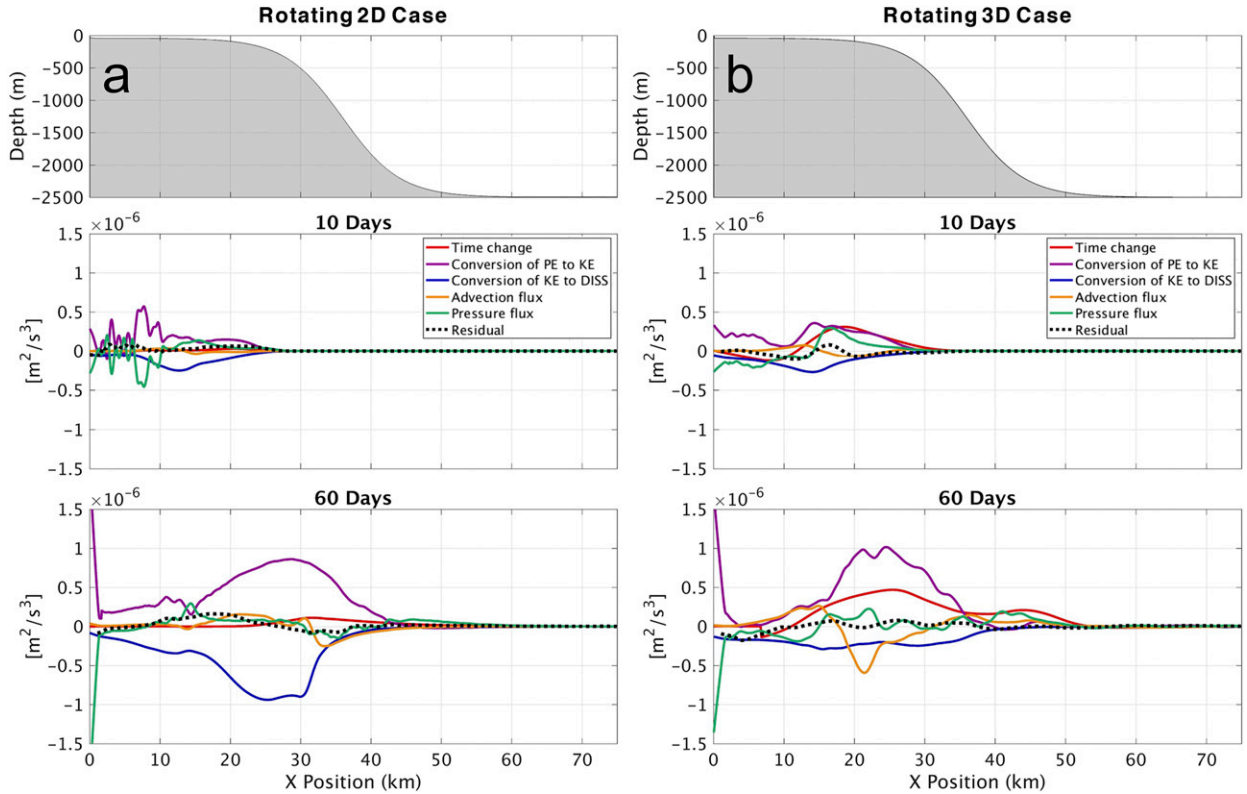


FIG. 18. Alongshore-averaged and depth-integrated terms of the kinetic energy budget according to Eq. (15) [with conversion terms described by Eqs. (16) and (17)]. The rotating (a) 2D SI-dominated case and (b) 3D eddy-dominated case with nominal forcing at 10 and 60 days.

in the Eurasian and Canadian basins are similarly stratified and forced during the fall and winter seasons, both in the initial sea ice formation phase and for ice-covered regions experiencing brine secretion (Cavaliere and Martin 1994). The continental slope magnitude is based on a Kara Sea transect (Rudels et al. 2000), with an average of 3.5° and maximum of 8° . Slopes around the Arctic are of similar scale (Jakobsson 2002). Although Arctic shelf widths reach hundreds of kilometers (our shelf was only 15 km), the majority of the dynamics occurs as the relatively homogeneous dense water moves off the shallow shelf and undergoes geostrophic adjustment. We hypothesize the dynamics will be fundamentally unaltered for a larger shelf, although the presence of dense water at the shelfbreak may be more transient and diluted. In the Antarctic, continental slopes similarly average 3° – 6° , and forcing conditions initiating dense shelf overflows (with vertical thicknesses ~ 300 m or less) have been observed, particularly in the Ross and western Weddell Seas (Baines and Condie 2013). Overflows forced by evaporation at intermediate latitudes may also be susceptible to analogous instability dynamics. More broadly, these results add to

the growing body of evidence emphasizing the role of submesoscale and frontal instabilities in the dissipation of balanced, geostrophic flows.

7. Summary

We have revisited the climatically significant problem of overflow dynamics, resolving the submesoscale range of motion. We focus our study on the vast Arctic shelves and examine three progressively complex scenarios—nonrotating 2D, rotating 2D, and rotating 3D—corresponding to different overflow regimes. The nonrotating 2D case behaves according to known theory. Gravitationally unstable water descends along the slope until reaching a level of neutral buoyancy within the uppermost 300 m of the water column, even for extreme forcing magnitudes. However, once rotation is added, the problem changes drastically; rotation confines shelf water laterally, allowing it to attain a larger density anomaly and become susceptible to a variety of instabilities.

We have identified novel dynamics in the rotating cases—in both 2D and 3D, the submesoscale range is

dominated by symmetric instability. In the 2D case, dense water flows offshore and undergoes geostrophic adjustment, forming a bottom-intensified jet and compensating surface-intensified jet. Ekman draining causes downslope descent of the lower jet, forming a highly dense alongslope front. SI is initiated, leading to vigorous mixing within the overflow. This regime applies for Arctic overflows in which the horizontal (alongslope) scales are below the baroclinic Rossby radius of deformation. In the 3D rotating case, geostrophic balance is broken by the onset of baroclinic instability, which leads to rapid downslope eddy transport of dense water. The character of the eddies is determined by forcing: strong forcing produces bottom-trapped eddies, while weak forcing (1/8 of the nominal value) leads to less-dense eddies propagating into the interior and attaining neutral buoyancy at intermediate depths. Although the 3D case is dominated by mesoscale eddies, there too is a strong signature of SI alongslope and at eddy edges.

Remarkably, we find that though they have very different dynamics, the rotating 2D and 3D cases lead to roughly the same final water mass distribution by density class. This result holds for all of the examined forcing magnitudes. In both regimes, buoyancy forcing cases corresponding to newly forming sea ice and strong atmospheric heat loss produce overflows ventilating the abyssal Arctic, while weaker forcing cases such as ice-covered regions that secrete brine slowly ventilate intermediate waters. For a given forcing magnitude, mixing in the SI-driven (2D) case is roughly the same as that in the eddy-driven (3D) case. In 2D, the mixing occurs through SI homogenizing negative Ertel PV regions, while in 3D, mixing occurs through the growth and vigorous volume entrainment initiated by baroclinic eddies. This is encouraging from the standpoint of modeling: magnitude of forcing, rather than model constraints, is the dominant factor determining final water mass characteristics. Although this study was idealized with respect to the Arctic, we believe the physical insights gained apply to a variety of overflow scenarios within the continental shelf regions of the real Arctic Ocean and worldwide. In subsequent work, we hope to study the contribution of SI to water mass modification and mixing relative to baroclinic eddies and address the need for its representation in larger-scale models.

Acknowledgments. We thank Robert Hallberg, Rong Zhang, and two anonymous reviewers for their thoughtful comments, and Stephen Griffies for insightful discussions on this work. This report was prepared by Elizabeth Yankovsky and Sonya Legg under Award NA14OAR4320106 from the National Oceanic and

Atmospheric Administration, U.S. Department of Commerce. The statements, findings, conclusions, and recommendations are those of the authors and do not necessarily reflect the views of the National Oceanic and Atmospheric Administration or the U.S. Department of Commerce. This material is based upon work supported by the National Science Foundation Graduate Research Fellowship under Grant DGE-1656466. Any opinions, findings, and conclusions or recommendations expressed in this material are those of the authors and do not necessarily reflect the views of the National Science Foundation.

REFERENCES

- Aagaard, K., L. Coachman, and E. C. Carmack, 1981: On the halocline of the Arctic Ocean. *Deep-Sea Res.*, **28A**, 529–545, [https://doi.org/10.1016/0198-0149\(81\)90115-1](https://doi.org/10.1016/0198-0149(81)90115-1).
- , J. H. Swift, and E. C. Carmack, 1985: Thermohaline circulation in the Arctic Mediterranean Seas. *J. Geophys. Res.*, **90**, 4833–4846, <https://doi.org/10.1029/JC090iC03p04833>.
- Allen, J. S., and P. A. Newberger, 1998: On symmetric instabilities in oceanic bottom boundary layers. *J. Phys. Oceanogr.*, **28**, 1131–1151, [https://doi.org/10.1175/1520-0485\(1998\)028<1131:OSHOB>2.0.CO;2](https://doi.org/10.1175/1520-0485(1998)028<1131:OSHOB>2.0.CO;2).
- Baines, P. G., and S. Condie, 2013: Observations and modelling of Antarctic downslope flows: A review. *Ocean, Ice, and Atmosphere: Interactions at the Antarctic Continental Margin*, S. S. Jacobs and R. F. Weiss, Eds., Antarctic Research Series, Vol. 75, Amer. Geophys. Union, 29–49, <https://doi.org/10.1029/AR075p0029>.
- Bergamasco, A., V. Defendi, E. Zambianchi, and G. Spezie, 2002: Evidence of dense water overflow on the Ross Sea shelf-break. *Antarct. Sci.*, **14**, 271–277, <https://doi.org/10.1017/S0954102002000068>.
- Brink, K. H., 2017: Surface cooling, winds, and eddies over the continental shelf. *J. Phys. Oceanogr.*, **47**, 879–894, <https://doi.org/10.1175/JPO-D-16-0196.1>.
- Cavaliere, D. J., and S. Martin, 1994: The contribution of Alaskan, Siberian, and Canadian coastal polynyas to the cold halocline layer of the Arctic Ocean. *J. Geophys. Res.*, **99**, 18 343–18 362, <https://doi.org/10.1029/94JC01169>.
- Eldevik, T., J. E. Ø. Nilsen, D. Iovino, K. A. Olsson, A. B. Sandø, and H. Drange, 2009: Observed sources and variability of Nordic seas overflow. *Nat. Geosci.*, **2**, 406–410, <https://doi.org/10.1038/ngeo518>.
- Gawarkiewicz, G., 2000: Effects of ambient stratification and shelfbreak topography on offshore transport of dense water on continental shelves. *J. Geophys. Res.*, **105**, 3307–3324, <https://doi.org/10.1029/1999JC900298>.
- , and D. C. Chapman, 1995: A numerical study of dense water formation and transport on a shallow, sloping continental shelf. *J. Geophys. Res.*, **100**, 4489–4507, <https://doi.org/10.1029/94JC01742>.
- Gula, J., M. J. Molemaker, and J. C. McWilliams, 2016: Topographic generation of submesoscale centrifugal instability and energy dissipation. *Nat. Commun.*, **7**, 12811, <https://doi.org/10.1038/ncomms12811>.
- Holton, J. R., 2004: *An Introduction to Dynamic Meteorology*. 4th ed. International Geophysics Series, Vol. 88, Academic Press, 535 pp.

- Hoskins, B. J., 1974: The role of potential vorticity in symmetric stability and instability. *Quart. J. Roy. Meteor. Soc.*, **100**, 480–482, <https://doi.org/10.1002/qj.49710042520>.
- Jakobsson, M., 2002: Hypsometry and volume of the Arctic Ocean and its constituent seas. *Geochem. Geophys. Geosyst.*, **3**, 1–18, <https://doi.org/10.1029/2001GC000302>.
- Killworth, P. D., 1983: Deep convection in the World Ocean. *Rev. Geophys.*, **21**, 1–26, <https://doi.org/10.1029/RG021i001p00001>.
- Legg, S., R. W. Hallberg, and J. B. Girton, 2006: Comparison of entrainment in overflows simulated by z-coordinate, isopycnal and non-hydrostatic models. *Ocean Modell.*, **11**, 69–97, <https://doi.org/10.1016/j.ocemod.2004.11.006>.
- Manucharyan, G. E., W. Moon, F. Sévellec, A. J. Wells, J.-Q. Zhong, and J. S. Wettlaufer, 2014: Steady turbulent density currents on a slope in a rotating fluid. *J. Fluid Mech.*, **746**, 405–436, <https://doi.org/10.1017/jfm.2014.119>.
- Marshall, J. C., and A. J. G. Nurser, 1992: Fluid dynamics of oceanic thermocline ventilation. *J. Phys. Oceanogr.*, **22**, 583–595, [https://doi.org/10.1175/1520-0485\(1992\)022<0583:FDOOTV>2.0.CO;2](https://doi.org/10.1175/1520-0485(1992)022<0583:FDOOTV>2.0.CO;2).
- , A. Adcroft, C. Hill, L. Perelman, and C. Heisey, 1997: A finite-volume, incompressible Navier Stokes model for studies of the ocean on parallel computers. *J. Geophys. Res.*, **102**, 5753–5766, <https://doi.org/10.1029/96JC02775>.
- McDougall, T. J., D. R. Jackett, D. G. Wright, and R. Feistel, 2003: Accurate and computationally efficient algorithms for potential temperature and density of seawater. *J. Atmos. Oceanic Technol.*, **20**, 730–741, [https://doi.org/10.1175/1520-0426\(2003\)20<730:AACEAF>2.0.CO;2](https://doi.org/10.1175/1520-0426(2003)20<730:AACEAF>2.0.CO;2).
- McIntyre, M. E., 1970: Diffusive destabilisation of the baroclinic circular vortex. *Geophys. Fluid Dyn.*, **1**, 19–57, <https://doi.org/10.1080/03091927009365767>.
- Molemaker, M. J., J. C. McWilliams, and W. K. Dewar, 2015: Submesoscale instability and generation of mesoscale anticyclones near a separation of the California Undercurrent. *J. Phys. Oceanogr.*, **45**, 613–629, <https://doi.org/10.1175/JPO-D-13-0225.1>.
- Murray, S. P., and W. Johns, 1997: Direct observations of seasonal exchange through the Bab el Mandab Strait. *Geophys. Res. Lett.*, **24**, 2557–2560, <https://doi.org/10.1029/97GL02741>.
- Pedlosky, J., 1992: *Geophysical Fluid Dynamics*. 2nd ed. Springer, 710 pp.
- Price, J. F., and Coauthors, 1993: Mediterranean outflow mixing and dynamics. *Science*, **259**, 1277–1282, <https://doi.org/10.1126/science.259.5099.1277>.
- Ruan, X., A. F. Thompson, M. M. Flexas, and J. Sprintall, 2017: Contribution of topographically generated submesoscale turbulence to Southern Ocean overturning. *Nat. Geosci.*, **10**, 840–845, <https://doi.org/10.1038/ngeo3053>.
- Rudels, B., R. D. Muench, J. Gunn, U. Schauer, and H. J. Friedrich, 2000: Evolution of the Arctic Ocean boundary current north of the Siberian shelves. *J. Mar. Syst.*, **25**, 77–99, [https://doi.org/10.1016/S0924-7963\(00\)00009-9](https://doi.org/10.1016/S0924-7963(00)00009-9).
- Shapiro, G. I., and A. E. Hill, 1997: Dynamics of dense water cascades at the shelf edge. *J. Phys. Oceanogr.*, **27**, 2381–2394, [https://doi.org/10.1175/1520-0485\(1997\)027<2381:DODWCA>2.0.CO;2](https://doi.org/10.1175/1520-0485(1997)027<2381:DODWCA>2.0.CO;2).
- , J. M. Huthnance, and V. V. Ivanov, 2003: Dense water cascading off the continental shelf. *J. Geophys. Res.*, **108**, 3390, <https://doi.org/10.1029/2002JC001610>.
- Taylor, J. R., and R. Ferrari, 2010: Buoyancy and wind-driven convection at mixed layer density fronts. *J. Phys. Oceanogr.*, **40**, 1222–1242, <https://doi.org/10.1175/2010JPO4365.1>.
- Thomas, L., J. Taylor, R. Ferrari, and T. M. Joyce, 2013: Symmetric instability in the Gulf Stream. *Deep-Sea Res. II*, **91**, 96–110, <https://doi.org/10.1016/j.dsr2.2013.02.025>.
- Turner, J. S., 1986: Turbulent entrainment: The development of the entrainment assumption, and its application to geophysical flows. *J. Fluid Mech.*, **173**, 431–471, <https://doi.org/10.1017/S0022112086001222>.
- Wirth, A., 2009: On the basic structure of oceanic gravity currents. *Ocean Dyn.*, **59**, 551–563, <https://doi.org/10.1007/s10236-009-0202-9>.
- Wobus, F., G. I. Shapiro, M. A. M. Maqueda, and J. M. Huthnance, 2011: Numerical simulations of dense water cascading on a steep slope. *J. Mar. Res.*, **69**, 391–415, <https://doi.org/10.1357/002224011798765268>.